Additive Manufacturing 56 (2022) 102905

Contents lists available at ScienceDirect

Additive Manufacturing

journal homepage: www.elsevier.com/locate/addma

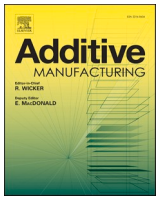

Research paper

On the design optimisation of direct energy deposited support structures to repair aero-engine turbine segments

N. D'Souza [a], S. Ravichandran [a], S. Donovan [a], P. Daum [a], R. Morrell [b], Z. Nye [c], R.J. Lancaster [c,*]

[a] Rolls-Royce Plc, PO Box 31, Derby DE24 8BJ, United Kingdom
[b] Engineering, Materials and Electrical Science Department, National Physical Laboratory, Hampton Road, Teddington, Middlesex TW11 0LW, United Kingdom
[c] Institute of Structural Materials, College of Engineering, Bay Campus, Swansea University, Swansea SA1 8EN, United Kingdom

ARTICLE INFO

Keywords:
Blown powder
Abradables
Cyclic behaviour
Flexural

ABSTRACT

A novel approach for down-selection of a repaired support structure design produced using Laser Blown Powder – Direct Energy Deposition (LBP-DED) and filled with interstitial Ni-Al powder (~0.75 area fraction) in a turbine segment was investigated. Simulation of flattening and un-flattening of the segment with implications to degradation of the support structure was quantified using a four-point bend test to identify the role of axial Young's modulus in out-of-plane flexure. Two markedly different LBP additive structures; Diamond Lattice (DL) - nodal and Continuous Path (CP) – non-nodal, were produced and compared with the un-repaired condition. At room temperature, the forward and rear walls and internal nodes of the original equipment (OE) and DL support structures were found to contribute significantly to the Young's modulus, with significantly reduced stiffness observed in the CP structures. Oxidation plays a key role in the development of internal compressive stresses within the abradable, with a two-fold increase in elastic modulus in the CP structure, but a smaller increase occurred in OE and DL support structures. A decrease in elastic modulus and concomitant increase in radius of curvature (flattening) occurred with an increasing number of flexural cycles. Cracking is most prominent in the nodal design within the front and rear walls and cracks propagate either to the surface or towards the base of the abradable lattice. No such degradation was observed for equivalent flexural cycles in the original and CP support structures, even up to a significant number of cycles. A criterion for catastrophic failure of the abradable was deduced from a steep decrease in flexural elastic modulus accompanied with a marked change in curvature. A non-nodal design support structure is optimum to counter in- service flattening/un-flattening.

1. Introduction

Additive manufacturing (AM), which involves creating or modifying a component through the addition of layers of material, is a versatile method used in numerous sectors such as biomedical, aerospace as well as automotive prototyping. Broadly, there are two types of AM metallic processes; (i) Powder Bed Fusion (PBF) processes, such as Laser Powder Bed Fusion (LPBF) and (ii) Directed Energy Deposition (DED) processes, such as Laser Blown Powder Direct Energy Deposition (LBP-DED), sometimes also referred to as laser deposition, blown powder additive, Laser Engineered Net Shaping (LENS), Laser Metal Deposition (LMD), Laser Cladding or Construction Laser Additive Direct (CLAD) [1]. Of the two, the DED process has a wide and promising range of applications in the manufacture of large components and in the repair of existing components. In DED, focused thermal energy is used to fuse materials by melting them as they are being deposited [2]. This is achieved by feeding wire or powder particles continuously into the melt pool formed by an energy source such as a laser, electron beam or arc. Relative motion of the heat source to the substrate generates the pre-designed configuration, which is referred to as the "laser deposition's or build structure's tool path".

Creation of successive layers in AM involves re-melting of some amount of the previous layer to ensure fusion of the successively deposited layers. On the one hand, rapid heating/cooling rates result in steep temperature gradients controlling the time interval between successive layers of deposition, while on the other, process parameters, such as laser power, spot size etc. influence the dynamics of the molten pool [3,4]. Both these factors affect the mechanical and microstructural properties of AM builds owing to the complicated thermal history experienced during the build process [5]. One focus in DED is the

* Corresponding author.
E-mail address: r.j.lancaster@swansea.ac.uk (R.J. Lancaster).

https://doi.org/10.1016/j.addma.2022.102905
Received 16 November 2021; Received in revised form 31 March 2022; Accepted 18 May 2022
Available online 21 May 2022

development of tailored microstructures for specific applications, characterised by the anisotropy of the mechanical properties, such as hardness, yield strength (YS) and ultimate tensile stress (UTS) [6–9]. A second application is in the creation of intricate lattice designs, specifically as in the case of open cellular (honeycomb) structures, where uniaxial compressive strength under monotonic and sometimes cyclic loading has been reported [10–14]. Notably, Yang et al. undertook a series of such tests, performing high cycle compression-compression fatigue experiments on a range of different LPBF lattice designs and found that a gradient structure offered a superior fatigue response compared to the uniform equivalent [15,16]. A third driver for the use of DED is repairing components. Saboori et al. [17] reported several case studies where the DED process has previously been used to repair numerous components found in a modern aerospace turbine engine, including bladed disks, or 'blisks', compressor blades, single crystal turbine blades and seal components. However, there is currently limited research available in the wider literature detailing the repair of a damaged abradable coating in a seal segment component, apart from patents previously collated by several of the current authors [18,19]. In a segment, the abradable feature is comprised of an open lattice structure with a Ni-Al filler alloy within the interstices. In the un-repaired (original equipment, OE) condition, the nickel alloy segment is manufactured by the investment casting route of directional solidification to produce a single crystal. The lattice is subsequently produced by plunge electro-discharge machining (EDM) and the interstices are then filled with Ni-Al powder and sintered. The function of the abradable is to prevent leakage of air by controlling turbine blade-tip clearance during engine running. This is achieved when the fins of a shrouded turbine blade cut tracks within the abradable. Following engine running, the repair process essentially involves re-building of the "worn-out" abradable structure on the segment by laser deposition. The typical sequence of operations in the repair process broadly involve; (i) removal of the worn-out abradable following engine-running using milling, (ii) additively building the support structure on the substrate (as-cast CMSX-3, Table 1) using LBP-DED with a Ni-base alloy feedstock, labelled Alloy X, which is a typical Ni-base superalloy with γ (Co, Cr and Mo) and γ′- (Al, Ta and Ti) phase stabilisers; and grain boundary strengthening elements; Hf, B and C, (iii) filling the interstices with Ni-Al powder, followed by (iv) sintering. Fig. 1 shows a segment with LBP-DED repaired abradable support structures, using a continuous support structure tool-path.

During service, the temperature difference between the hot gas-washed faces (abradable surface) and the cooled casing-side faces develops a radial thermal gradient across the segment, with a typical temperature difference of ~400 K. This thermal gradient gives rise to a shape change, where the segment effectively "flattens" (increased radius of curvature), like that occurring in a bimetallic strip. The key difference is that in the segment, a change in curvature arises from a radial temperature gradient while in the case of a bimetallic strip, the curvature arises from a difference in thermal expansion coefficient of the two constituents [20]. The integrity of the deposited abradable on the segment is therefore subject to the accumulated deformation occurring within the abradable during cyclic flattening/un-flattening of the segment under engine running and idle conditions. This is therefore equivalent to strain-controlled thermo-mechanical fatigue (TMF) behaviour. The residual stresses that develop within the abradable are dictated by the elastic modulus, given that segment flattening is essentially in the elastic domain. The elastic modulus is dictated primarily by the design of the abradable support structure, but the Ni-Al filler also plays a part. The principal aim of this paper will be therefore to design a simple test approach that will aid in down-selection of the most optimum abradable support structure design that minimises such residual stress during in-service flattening/un-flattening. The flattening/un-flattening of the segment and abradable in-service is akin to displacement controlled behaviour and can be well described by flexural bending, as in four-point bending. Under flexural loading, the degradation of the abradable occurs through vertical cracks, which will nucleate and propagate at stress concentrations in the support structure.

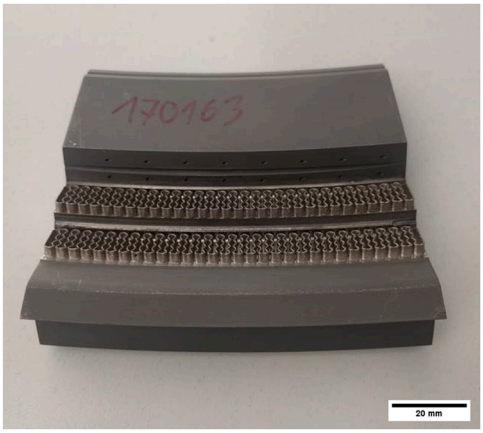

Fig. 1. A seal segment with the LBP-DED repaired abradable support structures, using a continuous support structure tool-path. No Ni-Al is present within the interstices.

While a rigorous study of these effects will involve carrying out detailed TMF tests on whole segments for a given design of the abradable support structure, such experiments are not straightforward even using non-standard geometries as well as being very expensive and time consuming and therefore beyond the scope of a low Technology Readiness Level (TRL) research project [21]. This study will investigate the properties of Original Equipment (OE) and laser deposited/repaired abradable support structures with different designs under flexural loading. Accordingly, the scope of this article encompasses the following objectives:

(1) To demonstrate the role of the support structure design and contribution of the sintered Ni-Al filler on the elastic modulus up to 1273 K (1000 °C), which approaches the operating temperature of the abradable.
(2) To carry out displacement-controlled flexural tests using four-point bending to quantitatively assess the different support structure designs to failure. The tests are carried out at room temperature (RT) to delineate the role of residual stress and are to be used solely as a comparator between two segment designs under similar displacement.

2. Experimental method

2.1. Laser blown powder – directed energy deposition (LBP-DED) process

The originally manufactured segment was single crystal and was investment cast via directional solidification using the state-of-the-art investment casting process. The LBP-DED process was used to additively repair the seal segment components and produce the test specimens. Fig. 2(a) is a schematic representation of the laser deposition

Table 1
Nominal composition (wt%) for CMSX-3.

Alloy	Al	Co	Cr	Ti	Mo	Ta	W	Si	Hf	B	C	Ni
CMSX-3	5.6	5	8	1	0.6	6	8	–	0.1	–	–	Bal.

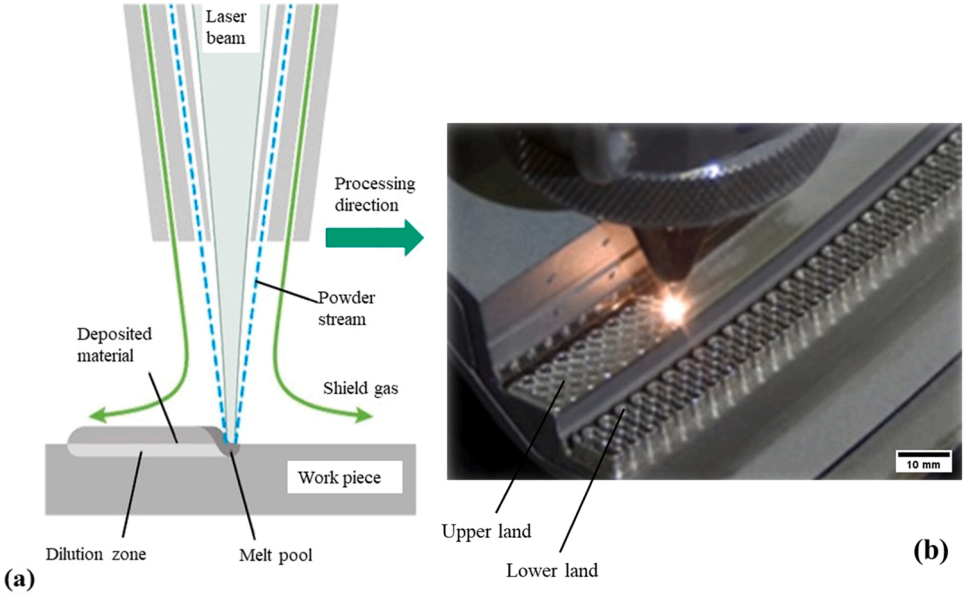

Fig. 2. (a) Schematic representation of the laser deposition process at the deposition head and substrate; (b) the first layer of the continuous path support structure being laser deposited on the upper land and the completed build on the lower land.

process at the deposition head and substrate. A continuous stream of powder feedstock blown out of the deposition nozzle is focused on the substrate surface where a laser beam impinges to create a melt pool. Melting of the underlying surface and the addition of powder forms a bead of deposited material on the substrate. Subsequent layers are added sequentially on top to build the support structure. Fig. 2(b) shows the first layer of the continuous path support structure being laser deposited on the upper land of the segment and the completed build on the lower land. The laser deposition tool paths are created from models of the support structure. CNC Cartesian based laser deposition systems control the laser deposition motion and programmed parameters. Two different seal segments types, whose arc lengths were 110 mm and 72 mm, were LBP-DED repaired using two different tool path support structure designs. The Diamond Lattice (DL) was designed to resemble the Original Equipment (OE) nodal design, containing continuous (long) forward and rear walls. The Continuous Path (CP) was designed to be less rigid, node free and with discontinuous forward and rear walls. Two different abradable arc lengths were considered; 110 mm long segments were repaired with both the DL and CP support structures, while only the DL design was evaluated on the 72 mm long support structure. Both structures were made of walls with a minimum thickness of ~ 300 μm. The LBP-DED process is extremely complex and affected by large number of variables. Intimate control of these variables is required to repeatably produce support structures of sufficient quality to meet engine service conditions. Key parameters utilised to achieve the build quality and geometric requirements included laser power, laser spot size, travel speed, process gas flow rate, and powder feed rate. Unfortunately, the specific quantifiable parameters are commercially sensitive, but the parameters utilized are consistent across all build geometries. Process controls include system calibration, monitoring and data logging of key variables, regular verification of parameters that cannot be monitored directly and the manufacture of separate process control test samples to verify the quality and internal soundness of the deposited structures. All LBP-DED builds were carried out using a single parameter set.

2.2. Test-piece preparation

Test-pieces of various types were prepared from original and repaired turbine seal segments of different sizes. The role of a nodal (diamond lattice – DL) versus a non-nodal (continuous path - CP) support structure was considered. Moreover, in the case of the latter, the front and rear walls are also missing and the support structure is comprised entirely of serpentine loops. A non-repaired baseline (DL) was also assessed. Table 2 shows the designations given in this paper to the different abradable types, based on the overall arc length. The width and height of the support structure for A1, B1 and C1 were ~10 mm and 2.5 – 2.7 mm respectively, while for B2, these were ~7 mm and 3.5 – 3.8 mm respectively.

The samples were extracted from the two types of segment using wire electro-discharge machining (EDM), forming a composite specimen comprising the underlying substrate and the abradable. The convex curved substrate face was then ground to an approximately constant thickness by hand grinding on a SiC flat paper. Excess width and length of substrate were similarly ground back to be closely level with the abradable walls. The top surface of the abradable was left in the as-manufactured condition. Oxidation of the Ni-Al in-fill material was performed either before EDM extraction or afterwards, in the latter case producing different outcomes owing to the relief of constraints within the abradable. In preliminary test-pieces the substrate thickness was reduced to between 0.25 and 0.45 mm, but in later tests, the maximum substrate thickness allowable by the segment cooling passage architecture was employed, which was typically 1.2–1.5 mm. There was also some variation in width of the test specimens, mainly in the case of Type A1 specimens, corresponding to the residual thickness of the long front and rear walls. Initial measurements of dynamic Young's modulus were made on OE specimens, where the front and rear walls were in the as-manufactured condition, but in later measurements the front and rear walls were trimmed so that only the nodal lattice was left on the substrate. This was however not the case with the Type C1 specimens,

Table 2
Abradable types evaluated.

Abradable type	Overall arc length 110 mm	Overall arc length 72 mm
Original manufacture (OE)	Type A1	–
DED - Diamond lattice repair	Type B1	Type B2
DED - Continuous path repair	Type C1	–

where the side-walls were absent. Type B1 and Type B2 specimens were left with the front and rear walls intact.

Quality standards used to evaluate the integrity of additively built parts and process control samples included; (i) visual inspection of external appearance (colour, smoothness, waviness and semi-adhered powder), (ii) external indications (voids, cracks, lack of fusion and presence of foreign material), (iii) geometric assessment of the built support structure for wall thickness, location and (iv) metallurgical evaluation of process control samples for both geometric and quality metrics (wall thickness (width), cracks, lack of fusion, porosity, voids, and depth of penetration).

2.3. Measurement of dynamic elastic modulus

The apparent dynamic Young's (elastic) modulus along the length of the abradable test-piece was measured following principles outlined in ASTM E1876, which employs the impact excitation method to determine the natural vibration frequencies of a prismatic beam [22]. The effect of the small level of curvature in the abradables was ignored. This is justified since the radius of curvature is greater than eight-times the thickness, permitting the use of straight flexural equations in ordinary beam bending which can be extended to beam vibration for modulus [23]. The mass of each specimen was measured on a calibrated electronic balance. The width and thickness were measured at three positions along each of the edges and the (chord) length was measured using calibrated Vernier callipers. The mass and averaged dimensional data were used for the calculation of elastic properties.

The measurements were made using a 1250HTVP facility manufactured by IMCE, Genk, Belgium. Room temperature (RT) measurements were made with the test-piece supported at 0.223 times the length from each end (i.e. at vibration nodes for the fundamental flexural mode) on nylon strings and struck centrally with a ceramic ball on a plastic strip. A microphone detects the emitted impact sound and a subsequent fast Fourier transform (FFT) determines the frequency spectrum. The apparent through-thickness (out-of-plane) flexural modulus of the composite test-piece is computed from the fundamental flexural mode frequency and the test-piece mass and dimensions, i.e. the test-piece is treated as a homogeneous body. This follows the procedure defined in [22]. Additionally, results for the in-plane flexural and longitudinal vibration directions were usually determined and are reported in some cases, but only for comparison, but these differ in value because of the composite structure of the test-piece.

The dynamic Young's modulus in the longitudinal direction corresponding to the flexural and longitudinal vibration modes is calculated using Eqs. (1a) and (2a) respectively [17];

$$E = 0.9465 \quad \left(\frac{mf_f}{b}\right) \quad \left(\frac{L}{t}\right)^3 T_1 \tag{1a}$$

where, E = Young's modulus (Pa), m = mass of bar (g), b, t and L are width, thickness and length of the test-piece respectively (mm), f_f = fundamental resonant frequency of bar (Hz) and T_1 = a correction factor for fundamental flexure to account for finite thickness and Poisson's ratio. The full form of T_1 is given in Eq. (3) in [22] and is initially of the form;

$$T_1 = 1 + 6.585(1 + + 0.0752\mu + 0.8109\mu^2)(t/L)^2.. \tag{1b}$$

For $L/t >> 20$, T_1 can be simplified to give;.

$$T_1 \approx [1 + 6{\cdot}585\ (t/L)^2]\ for\ L/t >> 20 \text{ for out-of-plane flexure mode} \tag{1c}$$

For the in-plane flexural mode, t and b are interchanged in Eq. (1a), as the test-piece is effectively rotated by 90°.

In the case of the longitudinal mode [22]:

$$E = 4 \quad m \quad f_l^2 \quad \left[\frac{L}{btK}\right] \tag{2a}$$

where, f_l = fundamental longitudinal frequency of bar (Hz) and K = correction factor to account for the finite diameter-to-length ratio and Poisson's ratio μ;

$$K = 1 - \left[\frac{\pi^2 \quad \mu^2 \quad D_e{}^2}{8 \quad L^2}\right] \tag{2b}$$

where D_e = effective diameter (mm) of the bar, which for a rectangular cross-section reduces to;

$$D_e{}^2 \quad = \quad \frac{2}{3} \quad (b^2 + \quad t^2) \tag{2c}$$

High temperature measurements were recorded in the controlled atmosphere furnace of the facility. The test-piece was suspended from a ceramic frame using nichrome wire suspension loops wound around it at 0.223 L from either end and struck from beneath using a remote ceramic impactor [22]. The emitted sound was detected by a microphone located outside of the furnace on the end of a ceramic tube waveguide positioned approximately 10 mm above the centre of the test-piece. Prior to measurements the furnace was evacuated twice and back-filled with Ar and the test was conducted in flowing Ar. Two heating/cooling runs were carried out at a nominal heating/cooling rate of 2 K s^{-1}. Like at RT, the apparent Young's modulus is calculated from the frequency spectrum corresponding to the fundamental flexural vibration mode. Again, the basic assumptions in the analysis were that the effect of the test-piece curvature on the vibrational response was minimal and that the material is homogenous and isotropic. The presence of anisotropy, as in the present case, implies that only an apparent shear (torsional) modulus can be determined so Poisson's ratio cannot be validly calculated. Table 3 gives the different sample pedigrees and conditions for the measurement of apparent dynamic Young's modulus corresponding to the preliminary measurements where the samples were not pre-oxidised. Table 4 presents results only for the abradable layer that has been deconvoluted from the composite using an elastic bilayer model assuming the elastic properties of the substrate from single crystal modulus data in the appropriate average orientation (as explained in Section 3). In the case of the latter measurements with thicker substrates, the segments were initially pre-oxidised in air at 1273 K (1000 °C) for 24 h and 100 h. Subsequently the abradables with underlying substrates were wire EDM'd from the segments for measurement of the elastic modulus. Some of these samples were subsequently also used in the low cyclic fatigue (LCF) tests outlined in the following section.

2.4. Flexural loading tests

The flexural loading cycles were performed under displacement control. Accordingly, an increasing imposed displacement was consid-

Table 3
Room temperature calculated apparent axial dynamic Young's modulus in different vibration modes corresponding to Types A1, Type B1 and Type C1 abradables with underlying substrate. Note that in this series of test-pieces the substrate thickness is typically 0.25 – 0.45 mm.

Specimen type and number	Apparent Young's Modulus along length of specimen (GPa)		
	Out-of-Plane Flexure	In-Plane Flexure	Longitudinal
Type A1, DE 001 (OE)	41.8	74.0	55.2
Type A1, DE 002 (OE)	52.8	84.3	59.5
Type A1, DE 003 (OE)	33.6	72.4	51.9
Type B1, DE 004	27.2	60.3	30.9
Type B1, DE 005	28.9	54.4	31.8
Type B1, DE 006	30.1	66.5	36.8
Type C1, DE 007	0.67	20.8	15.3
Type C1, DE 008	0.72	21.1	19.8

Table 4
Room temperature axial dynamic Young's modulus in different vibration modes corresponding to Types A1, Type B1 and Type C1 abradables with underlying substrate after sidewall modification. Note that in this series of test-pieces the substrate thickness is typically 0.25 – 0.45 mm. Also reported is the deconvoluted elastic modulus of the abradable only using Eq. (3).

Specimen type and number	Apparent elastic modulus along length of specimen, GPa			Deconvoluted apparent elastic modulus of the abradable-only for out-of-plane flexure, GPa
	Out-of-Plane Flexure	In-Plane Flexure	Longitudinal	
Type A1, DE001	38.3	72.1	53.3	18.6
Type A1, DE002	48.3	80.5	56.2	
Type A1, DE002[a]	40.7	69.2	51.7	21.5
Type A1, DE003	30.9	68.2	50.3	28.1
Type B1, DE004	26.4	54.6	29.2	13.8
Type B1, DE005	27.1	55.2	29.7	12.6
Type B1, DE006	29.4	62.2	35.0	13.1
Type C1, DE 007	0.63	17.0	14.2	0.16
Type C1, DE 008	0.76	15.1	15.1	0.18

[a] After further machining.

ered. For a given displacement, slow cycles preceded fast cycles to assess the accumulation of damage within the support structure. This was deduced from the maximum load, the slope of the load vs displacement curve as well as the net offset displacement at zero-load following unloading. The aim was to systematically assess the effect of increasing displacement on the cracking/degradation of the abradable. The abradable specimens were pre-oxidised in air at 1273 K (1000 °C) for 24 h and 100 h (Table 5) before extraction by EDM, where the thickness of the underlying substrate was typically between 1.0 and 1.5 mm. Testing was carried out in an Instron 4505 Universal Testing Machine equipped with a 10 kN load cell, using a non-articulating four-point flexure jig with laterally adjustable spans. A schematic diagram of the four-point test specimen is given in Fig. 3, where the load is applied on the substrate, while the support rollers are in contact with the abradable. The application of load results in flattening of the specimen, akin to what occurs in-service, owing to a thermal gradient. The quasi-static elastic modulus can be calculated by [24];

$$E = \left(\frac{F}{\delta} \right) \left(\frac{L^3}{8bt^3} \right) \quad (3)$$

where, F/δ is the slope of the load (F) – machine displacement (δ) trend, and L, b and t are the length, breadth and thickness of the specimen. In view of the low stiffness of the geometry, corrections for machine compliance have not been accounted for, for simplicity purposes.

For Type B2 specimens the inner/outer spans were adjusted to 34 mm and 68 mm respectively, while for specimens of Types A1, B1 and C1 the inner/outer spans were adjusted to 50 mm and 100 mm respectively. The test-piece was positioned with the abradable side face down and contacting the support rollers, with the loading rollers symmetrically located on the substrate back-face, as schematically illustrated in Fig. 3. This loading arrangement therefore simulates the flattening that would have occurred in the presence of a thermal gradient in service. Axial and lateral movement of the specimen on the loading rollers was restricted using small steel yokes located at the ends of the respective sizes of test-pieces. Sufficient gaps were allowed lengthwise to avoid restricting the flexure of the test-piece during loading. The wear of the abradable, which contacted the support rollers was minimised by taping small 0.5 mm thick spring steel pads on the abradable surfaces at both ends to act as bearing supports. The tests were performed under displacement control, rather than load control. This was to preclude early test termination from premature failure owing to unrealistic runaway displacements arising from degradation of the abradable during testing. Displacement control would therefore permit the tracking of accumulated degradation over a number of cycles. To do this, the following protocol was adopted.

Table 5
List of specimens and conditions for the flexural loading cyclic tests corresponding to Type A1, Type B2 and Type C1 abradables with underlying substrate. Substrate thickness is typically 1 – 1.3 mm.

Specimen Nomenclature	Displacement, δ (mm)	Number of Cycles	Condition
DED diamond lattice support structure – Type B2			
16 L	0.44	25,000	oxidised (1000 °C, 24 h)
16 U	0.60	25,000	oxidised (1000 °C, 24 h)
5 L	0.80	25,000	oxidised (1000 °C, 24 h)
5 U	0.80	25,000	oxidised (1000 °C, 100 h)
4 U	0.80	80,000	oxidised (1000 °C, 100 h)
23 U	1.10	20,000	oxidised (1000 °C, 100 h)
4 L	1.20	5000	oxidised (1000 °C, 100 h)
DED continuous path support structure - Type C1			
172_16U	1.50	40,000	oxidised (1000 °C, 100 h)
Un-repaired – Type A1			
RG8U	1.40	40,000	oxidised (1000 °C, 100 h)

* U and L refer to the front (upper - U) and rear (lower – L) abradables on a segment, as in Fig. 1.
* * For sample 16 L, following cyclic loading for 25,000 cycles at 0.44 mm displacement, monotonic loading was performed thereafter up to 0.9 mm displacement.

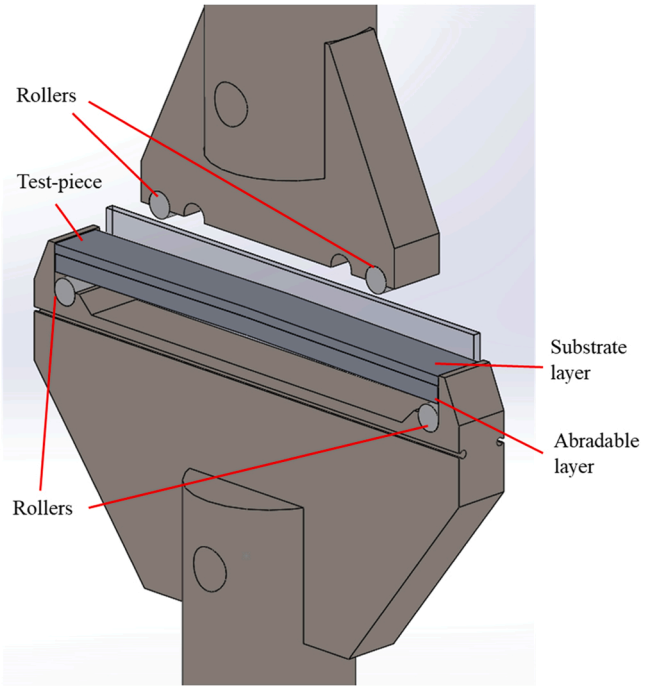

Fig. 3. Schematic diagram of the four-point bend test used for flexural testing of the abradable specimens.

(i) **Measurement of the dynamic elastic modulus of starting specimen** – Use impact excitation based on the approach defined in Section 2.2.

(ii) **Measurement of the specimen curvature** – Using a Nikon measuring microscope, measure the z-axis focus depth on the substrate face with a resolution better than $\pm$ 0.002 mm along the centre-line (x) of the substrate at 5 mm intervals. Then fit a best-fit polynomial curve to the displacements to obtain the equation for the curved surface; $R = 1/(d^2z/dx^2)$, where R = radius of curvature.

(iii) **Initial slow cycles for measurement of quasi-static loading elastic modulus** – Starting with zero-displacement make two slow (1 mm min^{-1} cross-head speed) loading cycles to the desired loading roller displacement, δ, to obtain force/displacement curves.

(iv) **Fast flexural cycles** – Carry out fast fatigue cycles (12 mm min^{-1} and 18 mm min^{-1} cross-head speeds for Type B2 and Types A1, B1, C1 respectively) up to a given number of pre-determined cycles.

(v) **Optical examination of side-walls** – Remove the specimen from the test machine and using an optical microscope examine the forward and rear walls (Type B2 and Type A1), as well as the outer surface of the abradables (all types) to assess for any damage/cracks. It must be emphasised that the examination of the support structure after each group of flexural loading cycles would preclude detailed sample preparation (mounting/polishing etc.), as would have been the case for a usual metallographic examination. This is because such preparation would have necessarily damaged the abradable before the next set of loading cycles in this interrupted testing method. Hence, examination of cracks was restricted to optical close-up views of cracks within rough surfaces at the end of each group of cycles. Moreover, since the onus was on the support structure, it was necessary to focus this region at the expense of the surrounding Ni-Al filler region and which consequently remains un-focused.

(vi) **Repeat steps (i) to (v) up to the next set of pre-determined group of cycles** – During each successive group of cycles, a change in specimen curvature develops. This results in an increasing period of complete off-loading resulting in a reduction in the true loaded deflection imposed by the machine. To circumvent this issue, the machine position at the onset of loading was re-adjusted to a "new zero position" after each group of cycles. This ensured that the originally required displacement was then re-applied for the start of the next group of loading cycles.

In initial experiments, the imposed peak deflection, δ was progressively increased starting with; $\delta = 0.44$ mm for Type B2 specimens, given that the typical average deflection during flattening in a thermal gradient during in-service conditions (and with a typical temperature difference of $\sim$ 400 °C from the cold face of the segment to the hot gas washed surface of the abradable operating at a temperature, $T = 1000$ °C) was in the range of; 0.39 – 0.55 mm. The maximum threshold deflection corresponded to the value above which there was a marked increase in radius of curvature accompanied by a steep decrease in Young's modulus. This corresponded to $\delta = 1.1$ mm for Type B2. In order to compare the two LBP-DED support structures (Types B and C), as well as the implications of LBP-DED repair (Type A and Type B), cyclic fatigue tests were carried out also for Type A and Type C specimens. However, since the span-length of the available Type B differed from Type A and Type C specimens, for a representative comparison, it is more appropriate to consider displacements that result in an equivalent change in curvature, ΔR. This was determined as the change in curvature occurring after the initial 1st and 2nd slow loading cycles. Furthermore, for expedience, comparison between Type B2 and the available Types A1 and C1 was only made with displacements corresponding to the threshold displacement for Type B2. Taking into account the greater span-length in Types A1 and C1, the machine deflection for Types A1 and C1 corresponding to $\delta = 1.1$ mm for Type B2 is (100/68) x 1.1 mm = 1.61 mm. A deflection of 1.5 mm was therefore applied to the loading rollers in C1. Accordingly, the change in curvature after the initial 1st and 2nd slow loading cycles was; $\Delta R = 385$ mm, compared with $\Delta R = 280$ mm (Type B2). The greater change in curvature for Types A1 and C1 compared with Type B2 allows a good comparison between the different cases. Tests were carried out up to a minimum number of 20,000 cycles and accordingly interrupted at 1000, 2000, 5,000 and 10,000 cycles. In some cases, tests were also conducted up to 25,000, 40,000 and 80,000 cycles to assess damage induced at higher numbers of cycles. Accordingly, an upper bound of the number of cycles for a given support structure were defined based on no further change in the maximum load or permanent flattening.

2.5. Measurement of change in specimen curvature from pre-oxidation

All abradable specimens in the flexural cyclic loading tests were pre-oxidised, which results in the development of residual stresses within the abradable. This is not straightforward to measure using conventional methods owing to the presence of the in-fill. A more qualitative approach, but yet very instructive, was used that focuses on the change in specimen curvature. The latter shape change arises from stress relaxation effects.

Specimen curvature was measured using a shadow graph. The specimens were clamped on the abradable lining side with the substrate facing upwards. This meant that the measured edge (the bottom of the substrate) would be as flat and consistent as possible for accuracy. Measurements were taken at equal intervals of 5 mm along the length, with the results displayed in Fig. 4. Effort was made to make each end of the specimen start at zero position to reduce the corrections needed in the data.

3. Results

3.1. Elastic modulus under different vibration directions

3.1.1. Room temperature tests

Initially, the elastic moduli of specimens with the abradable (height $\sim$2 – 2.7 mm) coating on a thin underlying substrate (thickness = 0.25–0.45 mm) were determined, since the aim was to calculate the elastic modulus of the abradable-only, by minimising the substrate thickness. Three pedigrees of specimens were considered, which following the terminology defined in Table 2 are; Types A1, B1 and C1. The plan-views of the abradables are presented in Fig. 5. In Type A1, Fig. 5(a), there clearly exists a variable thickness of the continuous front and rear walls where the lattice K-nodes intersect, depending on how the specimens are extracted from the segments. Consequently, the side-walls were trimmed to just expose the nodal lattice to overcome the issues with variable thickness; Fig. 5(b). This is not so in the case of Type B1; Fig. 5(c) where the re-built forward and rear walls can readily be retained in their entirety, and in the case of Type C1; Fig. 5(e) where there are no front/rear walls and the abradable support structure is surrounded by the sinter (Ni-AL) in-fill. The excess Ni-Al sinter ahead of the support structure was also removed in the LBP-DED case, as given in Fig. 5(d) and 5(f). Fig. 6(a) – (c) presents the FFT spectra for different vibration modes of the test-pieces where the sequence of peaks correspond to the sequence of vibration modes. Two key observations can be made;.

- There is more damping with diminished peak intensities observed in the LBP-DED abradable Type B1 and most significantly in Type C1 compared with the original manufacture Type A1.
- The peaks also shift to lower frequency, most noticeably in C1, indicating a decrease in modulus for broadly equivalent geometries.

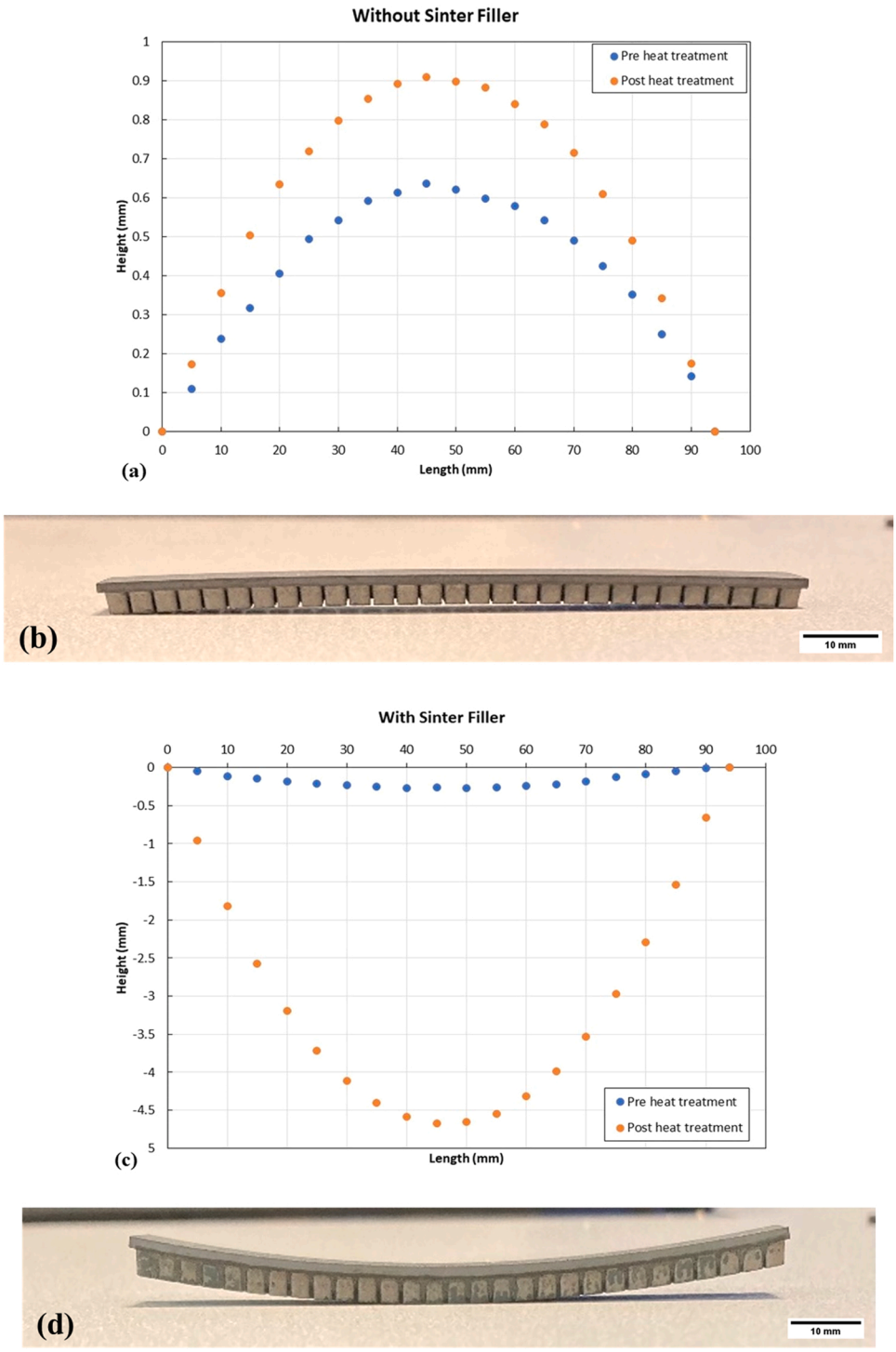

Fig. 4. Graphical and photographic representation of specimen curvature after pre-oxidation. (a) continuous path specimen without sinter filler increasing in curvature after oxidation, abradable lining on concave side of the strip, (b) visual representation of specimen without sinter filler, (c) continuous path specimen with sinter filler phase, specimen begins flat with abradable lining on convex side of strip, curvature increases during oxidation, abradable lining remaining on the convex side of the strip, (d) visual representation of specimen with Ni-Al sinter filler. Please note the y-axis different scales in (a) and (c).

Table 3 lists the calculated apparent axial dynamic Young's modulus corresponding to the different vibration directions. The following observations can be made;.

(i) The apparent Young's modulus for a given sample is dependent on the direction of vibration; it is lowest in out-of-plane flexure and greatest for in-plane-flexure, with the longitudinal mode intermediate.
(ii) The apparent Young's modulus in out-of-plane flexure in the case of Type C1 is an order of magnitude lower than Type A1 and Type B1 specimens.

The variation in elastic modulus primarily for Type A1, points to the important contribution of the front and rear wall thickness, which was variable along the length of the abradable; Fig. 5(a). Accordingly, to permit a consistent comparison, the excess material in the forward and rear walls was trimmed in Type A1; Fig. 5(b), while in Types B1 and C1, the excess Ni-Al sinter outside of the support structure was also removed; Fig. 5(d) and (f) respectively. Repeat measurements are given in Table 4 where the differences between test-pieces are markedly reduced, but also included is the de-convoluted elastic modulus of the abradable only.

If the properties of the substrate are known, it is possible to decon-

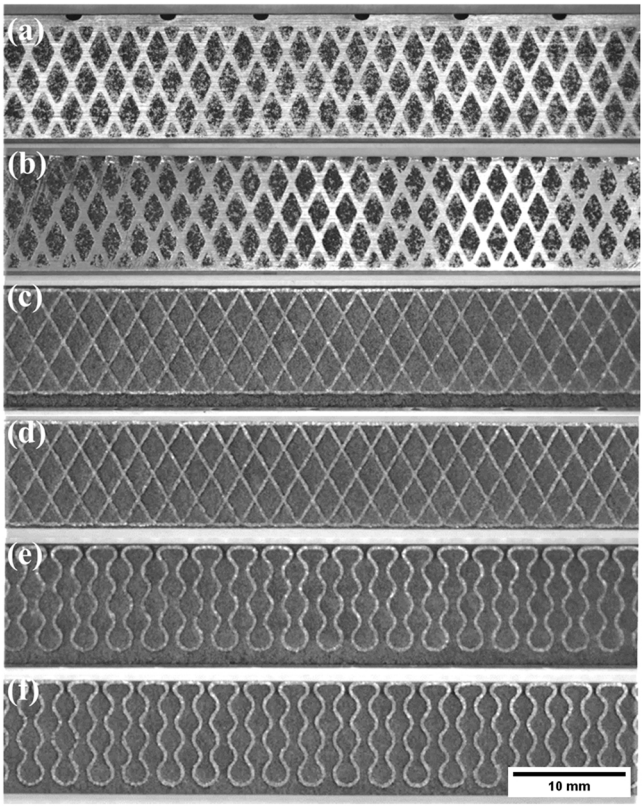

Fig. 5. Plan-view of the composite specimen (abradable and underlying substrate with thickness between 0.25 and 0.45 mm); (a) Type A1 specimen, (b) Type A1 specimen with trimmed forward and rear walls, (c) Type B1 specimen, (d) Type B1 specimen with excess Ni-Al sinter ahead of the support structure removed, (e) Type C1 specimen, (f) Type C1 specimen with excess Ni-Al sinter ahead of the support structure removed.

volute the elastic modulus attributable to the abradable structure alone. Since the principal mode of displacement of the abradable in service is out-of-plane flexure, which arises from thermal flattening of the segment in the presence of a radial thermal gradient, this calculation is performed for this vibration direction only. De-convolution in this case is achieved by using a two-layer coating model assuming the value of the modulus of the substrate alone, *Es*. The elastic modulus of the abradable layer, *Ec* is given by [25]:

$$E_c = \left[\frac{-A + \sqrt{A^2 + C}}{2R^3}\right] E_s \quad (4)$$

where, $R = \frac{t}{T}$, $F = (1+R)^3 \left(\frac{E_q}{E_s}\right)$, $A = 4R^2 + 6R + 4 - F$, $C = 4R^2(F - 1)$, t = thickness of abradable, T = thickness of the substrate and E_q = effective modulus of the test-piece treated as a whole and E_s = elastic modulus of substrate in the axial direction.

Using X-ray back-reflection Laue measurements, the Euler angles can be obtained from which the crystallographic orientation of the substrate along the length of the abradable and subsequently the elastic modulus can be calculated [26]. A key assumption is that in all the tests the effect of the test-piece curvature is neglected, since it has a minimal contribution to vibrational response. The Young's modulus of CMSX-3 (substrate) along the abradable length was calculated to be in the range; E_s = ~130 – 140 GPa. Accordingly, the calculated elastic moduli in out-of-plane flexure of the abradable (E_c) using Eq. (3) are reported in the last column of Table 4. In the composite specimen, the elastic modulus in out-of-plane flexure is two orders of magnitude lower for Type C1 compared with Type A1 and Type B1, with the latter two possessing 'reinforcing' forward and rear walls.

3.1.2. High Temperature Tests

Impact excitation was also used in high temperature tests across two heating/cooling cycles. Fig. 7(a) and (b) present the axial dynamic apparent elastic modulus in out-of-plane flexure across successive heating/cooling cycles for Type A1 in the fundamental flexural mode, while Fig. 7(c) and (d) present it for Type B1 specimens respectively. During first heating, the Young's modulus is near-constant up to typically 873 K (600 °C) for both specimens. For Type B1 there is a cusp observed between 873 K (600 °C) to 1073 K (800 °C) followed by a rise to 1273 K (1000 °C) and a decease thereafter to 1473 K (1200 °C). For Type A1, above 873 K (600 °C) there is an increase up to 1273 K (1000 °C) followed by a small decrease thereafter to 1473 K (1200 °C). During cooling the Young's modulus increases from 1473 K (1200 °C) down to RT. There is a marked difference in the Young's modulus between the first heating and subsequent cooling curves, with a near-two-fold increase in the Young's modulus during cooling. During the second heating cycle, the Young's modulus generally decreases up to 1473 K (1200 °C), but the cusp is still observed between 873 K (600 °C) to 1073 K (800 °C). During cooling, the Young's modulus increases down to RT. There is a markedly lower deviation between the second heating and cooling curves and only a small increase in Young's modulus on cooling compared with heating is observed.

Since the abradable is a composite structure comprised of a metallic lattice structure with Ni-Al powder packed within the interstices, the dependence of the Young's modulus on transient heating/cooling cycles indicates the role played by local sintering/oxidation effects occurring within Ni-Al as well as thermal expansion mismatch between Ni-Al and the support structure. Also, during service operation, the abradable would be in the oxidised condition, therefore making it pertinent to measure the elastic modulus of the abradable in the oxidised state. Consequently, all samples were subsequently pre-oxidised at 1273 K (1000 °C) for up to 24 h or 100 h. During expansile oxidation, residual strains develop leading to flattening of the extracted abradable specimen, especially when the substrate thickness is small, i.e. between 0.25 and 0.45 mm. Subsequently, a thicker substrate was retained; typically, up to 1.3 mm in the oxidised abradables. Also, high temperature apparent elastic modulus measurements on the LBP-DED build structure were carried out on abradables with smaller chord length, i.e. B2, as in Table 2, the reason being that this design, with build process parameters, as in Section 2.1, is used in subsequent flexural tests, rather than B1, when comparing with types A and C. Therefore, this design was used for measuring the high temperature apparent dynamic Young's modulus. Fig. 8 presents the apparent axial Young's modulus in out-of-plane flexure direction for composite (abradable + substrate) specimens of Types A1, B2 and C1 over successive heating/cooling cycles between room temperature (RT) and 1273 K (1000 °C). Fig. 8(a), (b) refer to Type A1 over the 1st and 2nd heating/cooling cycles respectively, Fig. 8 (c), (d) correspond to Type B2 over the 1st and 2nd heating/cooling cycles respectively and Fig. 8(e), (f) pertain to Type C1 over the 1st and 2nd heating/cooling cycles respectively. It should be noted that the typical substrate thickness in these specimens varied between 1 and 1.3 mm, unlike in the earlier experiments summarised in Tables 3A and 3B. Again, the fundamental flexural vibration mode was used, as in Fig. 7(a) and (b). In Type A1, hysteresis is observed (~5 GPa) in the first heating/cooling run, but in the second heating/cooling cycle this is markedly lower (~2 GPa). A kink was also observed during both heating and cooling at 523 K (250 °C). In the Type B2 specimen, slight hysteresis is observed (~1 GPa) in the first heating/cooling run, but this is absent in the second heating/cooling run. Again, a kink is observed during both heating and cooling at 523 K (250 °C). Finally, in the Type C1 specimen, a marked difference is observed. A maxima is observed typically between 473 K (200 °C) and 673 K (400 °C), but thereafter there is an increase in Young's modulus. A difference of ~5 GPa is observed between heating/cooling runs, with a larger value obtained on cooling. Therefore, while in the case of Type A1 and Type B2 an expected variation in apparent elastic modulus similar to that in Fig. 5(a) and (b) is

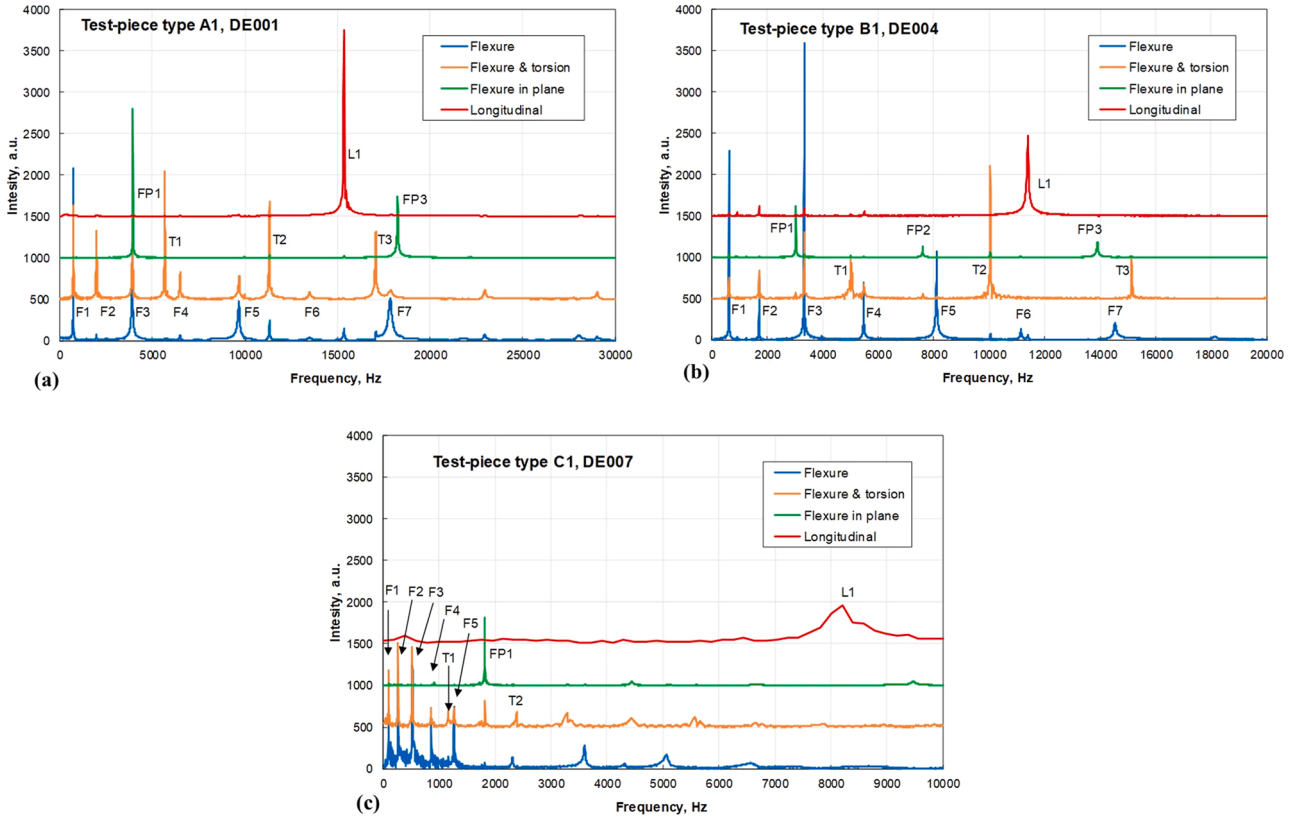

Fig. 6. Room temperature (RT) fast Fourier transform frequency spectra for different vibration modes; *Fn*, out-of-plane (through-thickness) flexural mode peaks, *FPn*, in-plane flexure mode peaks and *Ln*, longitudinal mode peaks of abradable with underlying substrate; (a) Type A1 (OE), (b) Type B1 (c) Type C1.

observed, a marked difference exists in the Type C1 specimen. The key aspect is that the measurements correspond to the composite structure, i.e. abradable and substrate, but the abradable is also a composite and comprises metallic support walls and Ni-Al powder in the interstices, both of which oxidise to some degree. In order to address the role of oxidation, Fig. 9(a) presents a back-scattered electron image showing two fingers of the support structure, while Fig. 9(b) and (c) correspond to Ni and O EDS maps from spectra acquired in this region. It can be seen that there is a recession of the support structure walls because of oxidation, while oxidation of Ni-Al filler also occurs, following from Fig. 9(c). The oxides are typically; (Ni Co), spinels ($NiAl_2O_4$) and Al_2O_3. The implication of these factors on the apparent elastic modulus will be examined in the discussion section.

3.2. Displacement controlled flexural loading cycles

The four-point bend tests were carried out under displacement control at room temperature (RT). Force vs displacement curves have been used to assess the degradation of the abradables across all designs, rather than convert these to stress vs strain. There are reasons for not attempting the latter. First, the arc length of all abradables (A1, B1 and C1, Table 1) were the same and when the arc length was smaller, as in case of B2 (Table 2), the displacement was appropriately scaled to give an equivalent displacement to the longer arc length abradables. Second, it is also more meaningful to consider displacements, since this parameter is relevant for deflection of the abradable owing to a temperature gradient in-service. Finally, owing to the sandwich (CMSX-3 substrate and abradable) structure, the through-thickness elastic modulus is only an "effective" modulus. It provides a very good criterion for comparison of the different designs during flexure, but less relevant as an elastic modulus per se for the calculation of stress from strain.

Two slow loading/unloading (1 mm min^{-1}) cycles preceded the fast loading/unloading cycles, such that the load-displacement plot under quasi-static conditions can be examined. The samples have been oxidised at 1273 K (1000 °C) for 24 h and 100 h, to overcome the effect of oxidation, as observed in the hysteresis in Fig. 7(a) – (d), in the absence of pre-oxidation. Table 5 lists details of the various flexural tests, which comprises the oxidation conditions, the imposed deflection at the loading rollers and the number of loading cycles. Fig. 10 presents the measured apparent dynamic Young's modulus in out-of-plane flexure mode at RT between successive groups of fatigue cycles under zero-load corresponding to; Type A1, Type B2 and Type C1 specimens.

The results show that in the Type B specimen, for a displacement (δ) of 0.44 mm $< \delta \leq$ 0.8 mm, there is an initial decrease in apparent elastic modulus, after which there is no noticeable decrease in elastic modulus up to 25,000 cycles. Specifically, for a displacement, $\delta = 0.8$ mm, a continual decrease in elastic modulus occurs ($\sim$ 18–20 GPa occurs up to 20,000 cycles). Then between 20,000 and 80,000 cycles, the decrease in elastic modulus is $\sim$ 4 GPa. When the same specimen type if subjected to displacements of 1.1 mm and 1.2 mm, a steep decline in apparent elastic modulus occurs after 5 cycles and 1000 cycles respectively. For $\delta = 1.1$ mm, the decrease in elastic modulus is $\sim$ 27 GPa which occurs over 10,000 cycles, at which point the test was terminated, while for $\delta = 1.2$ mm, the decrease in elastic modulus is $\sim$ 30 GPa which takes place over 5000 cycles (test terminated). In the Type A1 specimen, for $\delta = 1.5$ mm, there is an initial drop in elastic modulus of $\sim$ 15 GPa, followed by a near-constant elastic modulus up to 40,000 cycles thereafter. For Type C1, a small drop in elastic modulus was observed ($\sim$ 5 GPa) over 40,000 cycles for $\delta = 1.5$ mm.

The apparent dynamic elastic modulus of the composite specimens presented in Fig. 10 corresponds to zero-load and is measured between successive groups of flexural cycles. On the other hand, the quasi-statically loaded flexural modulus can be measured from two slow loading cycles that precede the fast cycles. Fig. 11 presents the load-

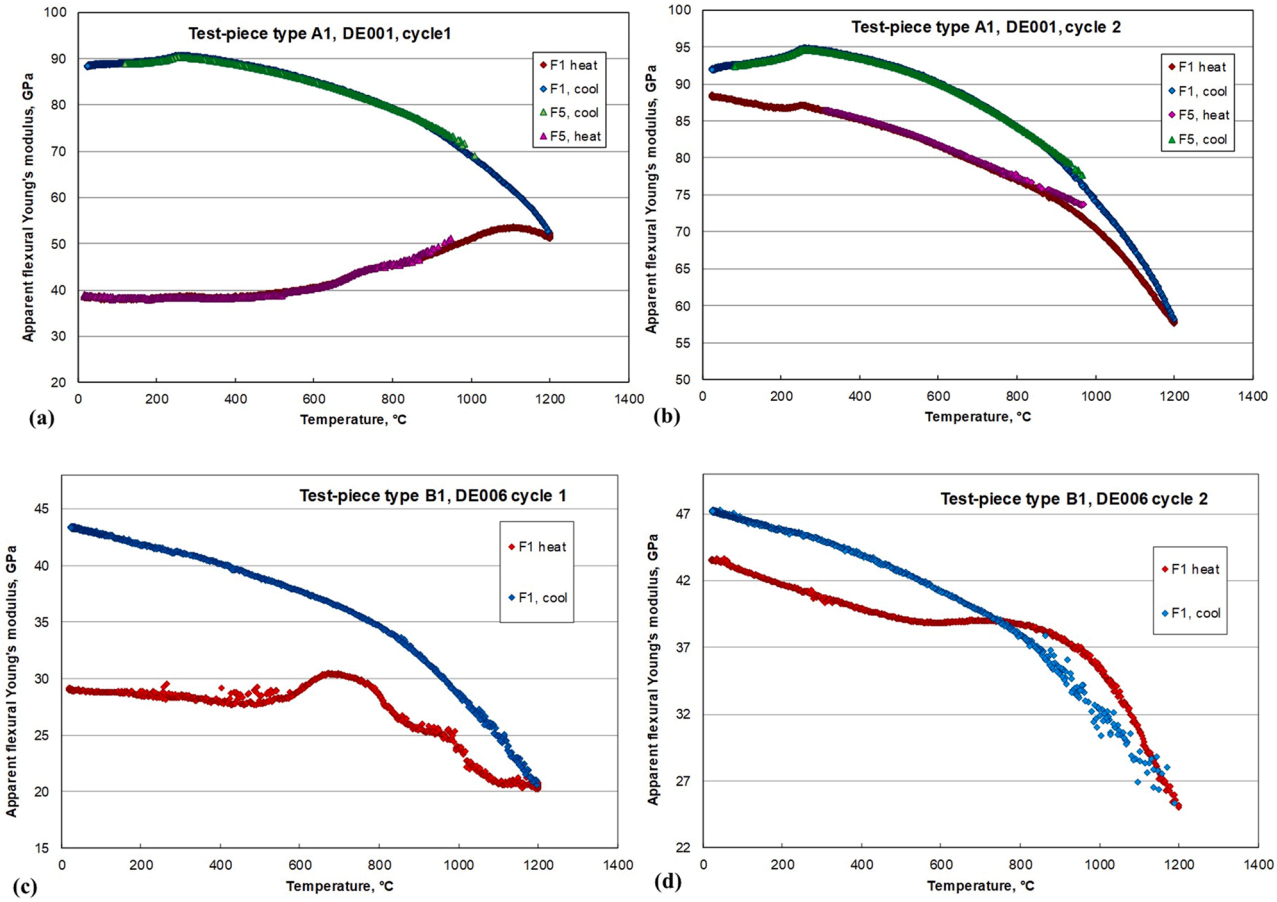

Fig. 7. Apparent axial Young's modulus of the abradable and underlying substrate (0.25–0.45 mm thickness) in out-of-plane flexure direction across two heating/cooling cycles between room temperature (RT) and 1473 K (1200 °C); (a) Type A1 – 1st heating/cooling, (b) Type A1 – 2nd heating/cooling, (c) Type B1 – 1st heating/cooling, (d) Type B1 – 2nd heating/cooling.

displacement graphs for slow loading/unloading cycles at the commencement of successive groups of flexural cycles for two typical displacements. These correspond to, $\delta = 0.8$ mm and 1.1 mm respectively (Type B2), where there is a marked difference in the evolution of the dynamic elastic modulus with an increasing number of fatigue cycles. Here; (a), (b) - cycles 1 and 2, (c), (d) - cycles 1001 and 1002, (e), (f) - cycles 20,001 and 20,002. (a), (c) and (e) refer to #5 U ($\delta = 0.8$ mm) and (b), (d) and (f) refer to #23 U ($\delta = 1.1$ mm). The displacement is greater than zero when load equals zero following un-loading, owing to the next flattening (permanent deformation) of the specimen. This will be addressed in Fig. 13 (a) – (d).

Fig. 12(a) and (b) present the calculated quasi-static elastic modulus for #4 U and #23 U respectively over two successive slow loading cycles. The results are shown for the lower loading range (50–150 N) and higher loading range (350–450 N), since the load vs cross head displacement graphs in Fig. 10 is not linear across the entire loading range. Also included is the dynamic elastic modulus from impact excitation in the unloaded condition. The results show that there is a permanent offset displacement at the end of the 1st unloading cycle but is markedly lower at the end of the 2nd unloading cycle. This incremental permanent offset displacement decreases with an increasing number of fatigue cycles, i.e. 1001/1002 and 20,001/20,002 cycles and is also greater for the higher imposed displacement. Owing to the change in slope during loading, the quasi-static elastic modulus varies across the loading range, where there is generally an overall decrease in elastic modulus with increasing fatigue cycles for a given loading range and the quasi-static moduli are significantly lower than those measured under the zero-load condition.

The variation in the gradient of the slope in the load-displacement plot coupled with the permanent offset displacement is a result of stress relaxation that occurs during successive loading cycles, as indicated by the decrease in elastic modulus. This permanent offset that develops manifests as a change in shape of the specimen and can be quantified by characterising the test-piece back-face height, which is related to the curvature of the abradable, between successive groups of fatigue cycles. Fig. 13(a) - (d) plot the test-piece back-face height after successive groups of flexural cycles corresponding to different imposed displacements; $\delta = 0.8$ mm (#4 U), 1.1 mm (#23 U) and 1.2 mm (#4 L) for Type B2 and 1.5 mm for Type C1 (#172_16U) respectively. The results show that there is a change in curvature of the specimen after oxidation before imposing any displacement on either abradable geometry. The corresponding increase in radius of curvature is typically; $\Delta R = 115 - 160$ mm. In the Type B2 specimens, there is a rapid "flattening" (increasing radius of curvature) that occurs beyond a threshold number of fatigue cycles with increasing magnitude of displacement. For $\delta = 0.8$ mm flattening is gradual, but for $\delta = 1.1$ mm a marked increase in radius of curvature occurs between 1000 and 2000 cycles and for $\delta = 1.2$ mm this occurs between 5 and 1000 cycles. Further, the development of asymmetry in shape of the abradable specimen along its length indicates inhomogeneous deformation. In the case of Type C1 specimens, while there is a marked flattening after oxidation, thereafter a negligible amount of permanent flattening during loading is observed.

It is important to note that the marked change in curvature of the Type B2 specimens subjected to $\delta = 1.1$ mm and 1.2 mm is also consistent with the rapid decrease in Young's modulus, as shown in Fig. 10. The decrease is consistent with the accumulation of deformation

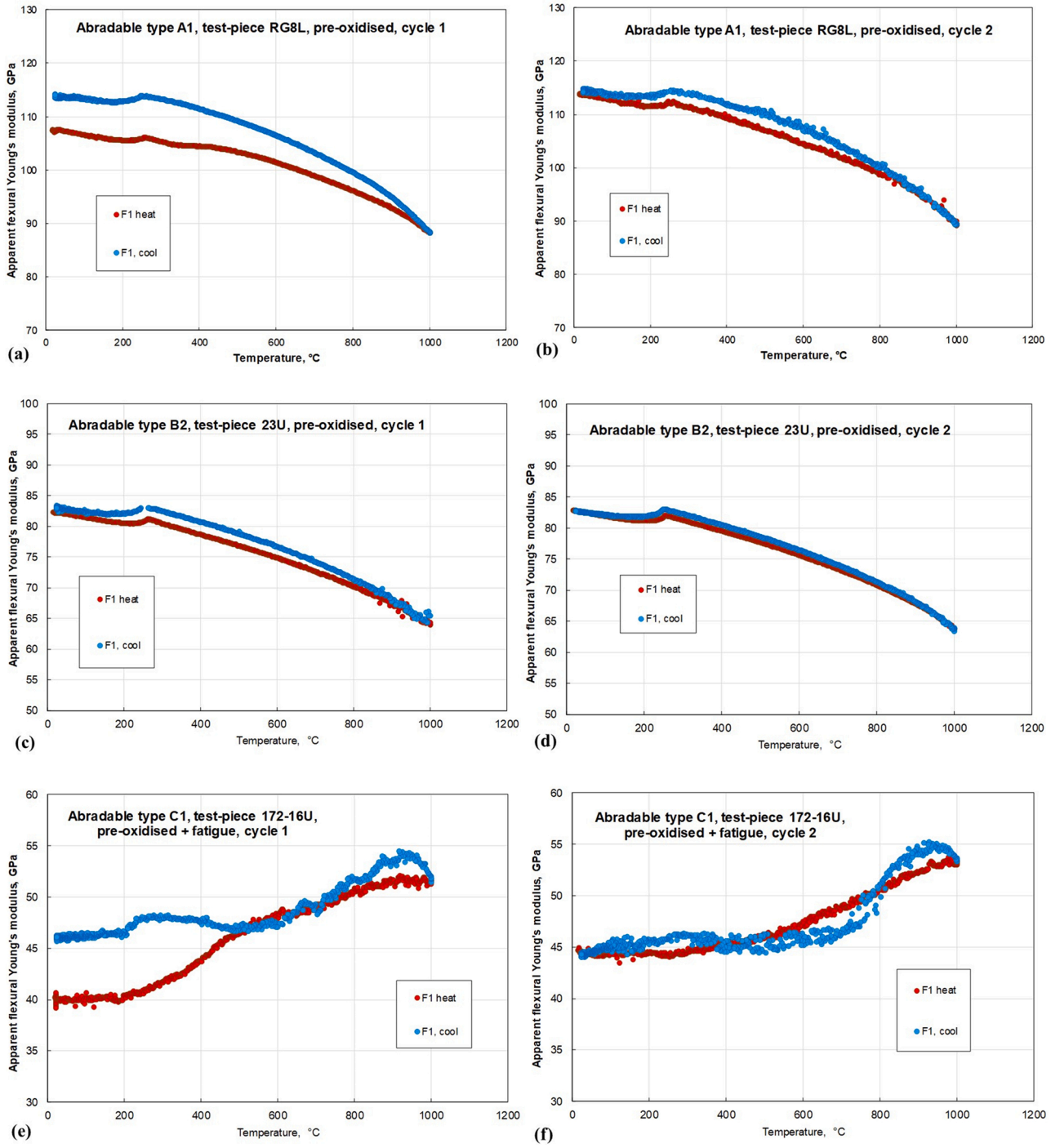

Fig. 8. Apparent axial Young's modulus in out-of-plane flexure direction for composite (abradable + substrate) specimens of Types A1, B2 and C1 over successive heating/cooling cycles between room temperature (RT) and 1273 K (1000 °C); (a), (b) refer to Type A1 over the 1st and 2nd heating/cooling cycles respectively, (c), (d) corresponds to Type B2 over the 1st and 2nd heating/cooling cycles respectively, (e), (f) pertain to Type C1 over the 1st and 2nd heating/cooling cycles respectively. Substrate thickness is 1 – 1.3 mm.

within the Type B2 abradable during fatigue.

3.3. Deformation within the support structure

The deformation was examined within the Type B2 specimens, where maximum degradation was observed. A detailed inspection of the forward and rear walls and internal lattice was carried out and some representative examples are presented. Fig. 14(a) and (b) correspond to a location on the side-wall, 5.8 mm to the right of the centre for #4 L ($\delta = 1.2$ mm), after 2000 and 5000 fatigue cycles respectively. Fig. 15 (a) and (b) correspond to a location on the side-wall 6.5 mm to the right of the centre for #4 L ($\delta = 1.2$ mm) after 2000 and 5000 fatigue cycles respectively. Similarly, Fig. 16(a) – (d) refer to #5 L ($\delta = 0.8$ mm) and show the internal lattice structure after 10,000 cycles, both in the vicinity of K-nodes (at the wall) and X-nodes (internal lattice). The forward/rear walls can be seen to contain discontinuities on either side of some of the K-nodes. These are either closed curved shrinkage fissures running broadly upwards towards the top surface of the abradable or a

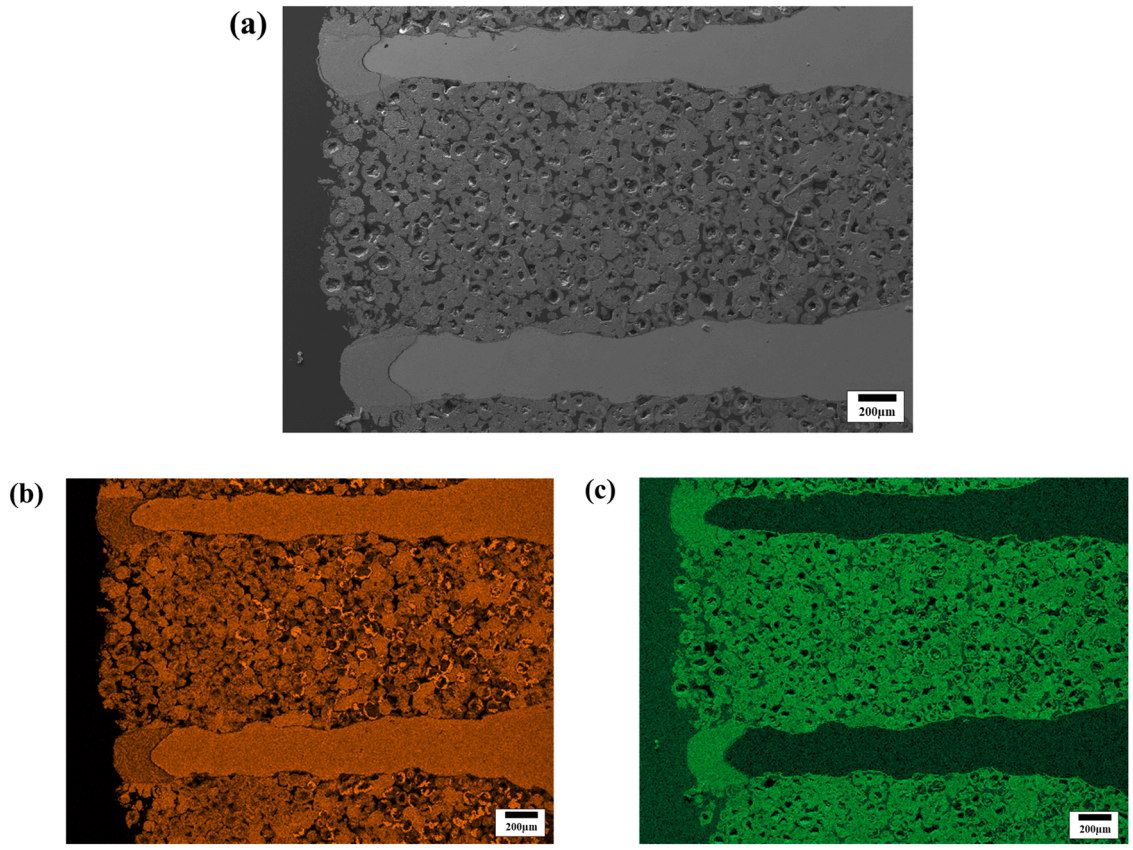

Fig. 9. Examination of oxidation of abradable after exposure at 1273 K (1000 °C) for 100 h; (a) back-scattered electron image (BEI), energy dispersive X-ray spectroscopy (EDS) maps for (b) Ni and (c) O.

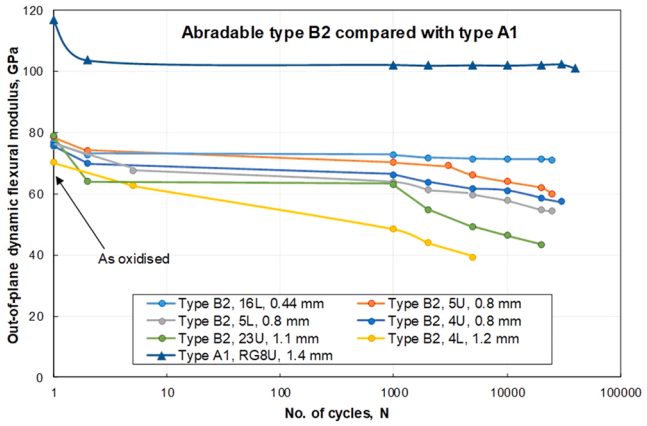

Fig. 10. Apparent axial Young's modulus in out-of-plane flexure direction at room temperature (RT) after successive groups of fatigue cycles measured under zero-load conditions for abradable samples with underlying substrates subjected to different flexural fatigue displacements; Type A1, Type B2 and Type C1. They have all been pre-oxidised at 1273 K (1000 °C) for 24 h or 100 h.

series of fissures lying one above the other. Porosity is observed within these regions and indicates that these are shrinkage related. Fine cracks are seen to develop from the ends of fissures with an increasing number of fatigue cycles. These can be broadly classed as:

- When fissures originate close to the upper abradable surface, cracks emanating from the upper end of a closed fissure propagate to the top of the wall.
- Cracks also nucleate below the lower ends of shrinkage fissures already connected to the top edge of the abradable wall and with increasing number of cycles grow towards the base of the abradable.
- Cracks tend to link adjacent fissures. When two fissures are located in the proximity of each other vertically, cracks emanating from each fissure concatenate.

Cracking within the internal lattice X-nodes that propagate to the top of the lattice is only observed very sporadically, indicating that the diamond lattice is relatively undamaged and deformation is primarily concentrated within the forward/rear walls. In contrast, there was no observed damage in either Type A1 or Type C1 specimens apart from some cracks visible through the sintered Ni-Al powder in the latter.

Fig. 17(a) and (b) present two alternative views of the same crack face; (a) referring to the face with the crack in plan-view at a front/rear supporting wall and (b) representing a side-view of the front/rear walls at the K node. Fig. 17(a) shows that owing to pre-oxidation at 1000 °C for 100 h, it is very difficult to noticeably discern any prominent crack propagation paths from simple fractography. Along the inside face of the crack there is considerable oxide build-up, as denoted by the region within the yellow curve. Along many of the K nodes along the front/rear walls of the support structure there are vertical cracks propagating from the top of the wall. Fig. 17(b) shows the length and geometry of a typical crack at a K node, clearly indicating it has developed at a certain location at the top of the support structure front/rear wall and subsequently propagated downwards towards the substrate during flexural testing.

As can be seen in Fig. 18(a), there are many pores present within the front/rear walls at the K nodes, acting as potential crack initiation sites. Propagation then occurs through concatenation of the micro-pore features. This is further highlighted in Fig. 18(b), which shows a high magnification image of these pores coalescing. Fig. 18(c) is a secondary

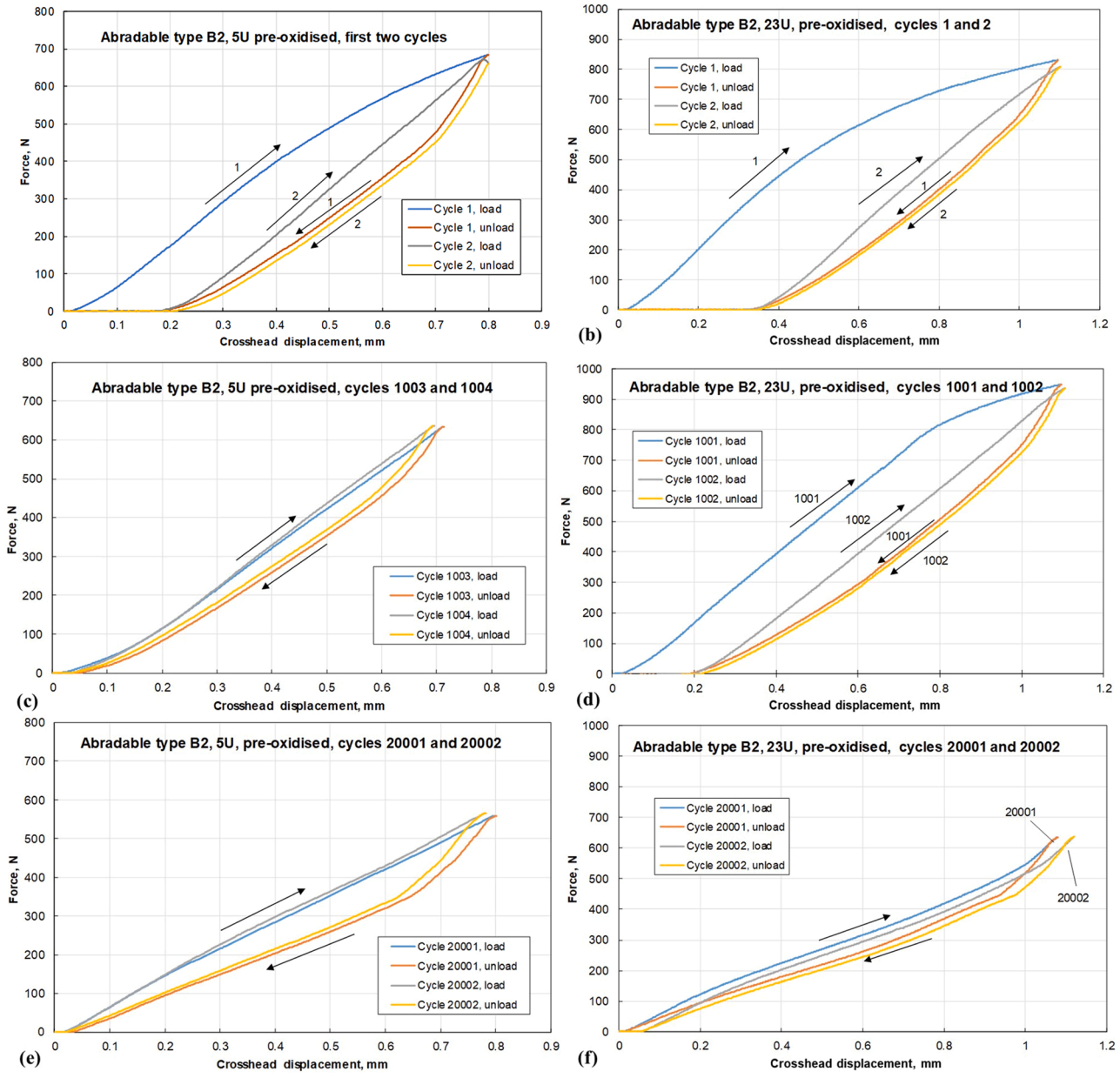

Fig. 11. Load-displacement graphs for slow loading/unloading cycles (1 mm min^{-1}) before commencement of successive group of flexural cycles (12 mm min^{-1}) for Type B2; (a), (b) - cycles 1 and 2, (c), (d) - cycles 1001 and 1002, (e), (f) - cycles 20,001 and 20,002. (a), (c) and (e) refer to #5 U; $\delta = 0.8$ mm and (b), (d) and (f) refer to #23 U; $\delta = 1.1$ mm.

electron image of a portion of the support structure wall, highlighting the cellular solidification structure. However, as argued, the propagation of the cracks can be adequately followed by a more mesoscopic based analysis as has been shown in Fig. 18(a) and (b).

4. Discussion

The basic assumption in the impact excitation method used to measure the apparent dynamic elastic modulus of a prismatic beam from the natural frequencies of vibration is that the sample is homogeneous and isotropic. The substrate is homogeneous and while a slight curvature exists along the length of the specimen (maximum height of backface = 1 – 1.5 mm across a length of ~ 70 – 100 mm), this small curvature can be ignored. By using Laue back-reflection and measurement of the crystallographic angles α and ρ within the substrate along the axial length of the abradable, the elastic modulus of the substrate can be calculated from the single crystal elastic constants using Eq. (4) [27,28]. However, there is also lack of homogeneity within the abradable owing to the existence of the Ni-Al powder. This latter factor is principal reason for the dependence of the apparent dynamic elastic modulus on the direction of vibration; being the lowest in out-of-plane flexure and greatest for in-plane flexure. This is unlike that for a homogenous isotropic solid, where the elastic modulus should be independent of the direction of vibration. Since the axial elastic modulus of the substrate (~127 GPa) is much greater than that of the abradable (0.16–28.1 GPa), it is clear from Tables 3 and 4 that the contribution of the substrate to the effective elastic modulus is greatest for in-plane flexure and least for out-of-plane bending. Therefore, the elastic modulus of the composite specimen in out-of-plane flexure is influenced primarily by the "less-stiff" abradable. The other key aspect relates to the implications of abradable design to the elastic modulus in out-of-plane flexure. It can be deduced that in the case of the diamond lattice (Types A1, B1 and B2), the axial elastic modulus is primarily dictated by the forward and rear walls and the internal nodal structure, both of which are absent in Type C1 resulting in

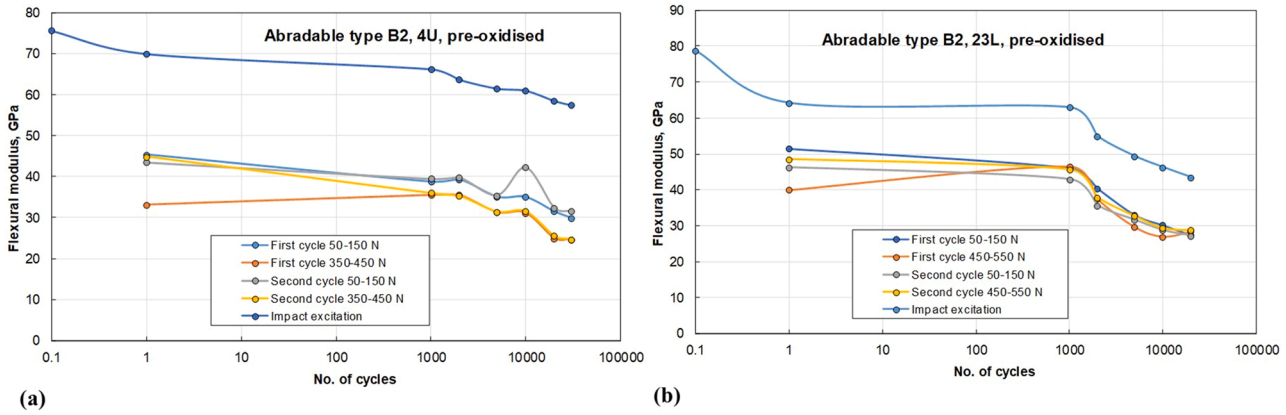

Fig. 12. Calculated quasi-static elastic modulus respectively over two successive loading cycles for Type B2; (a) #4 U; $\delta = 0.8$ mm, (b) #23 U; $\delta = 1.1$ mm.

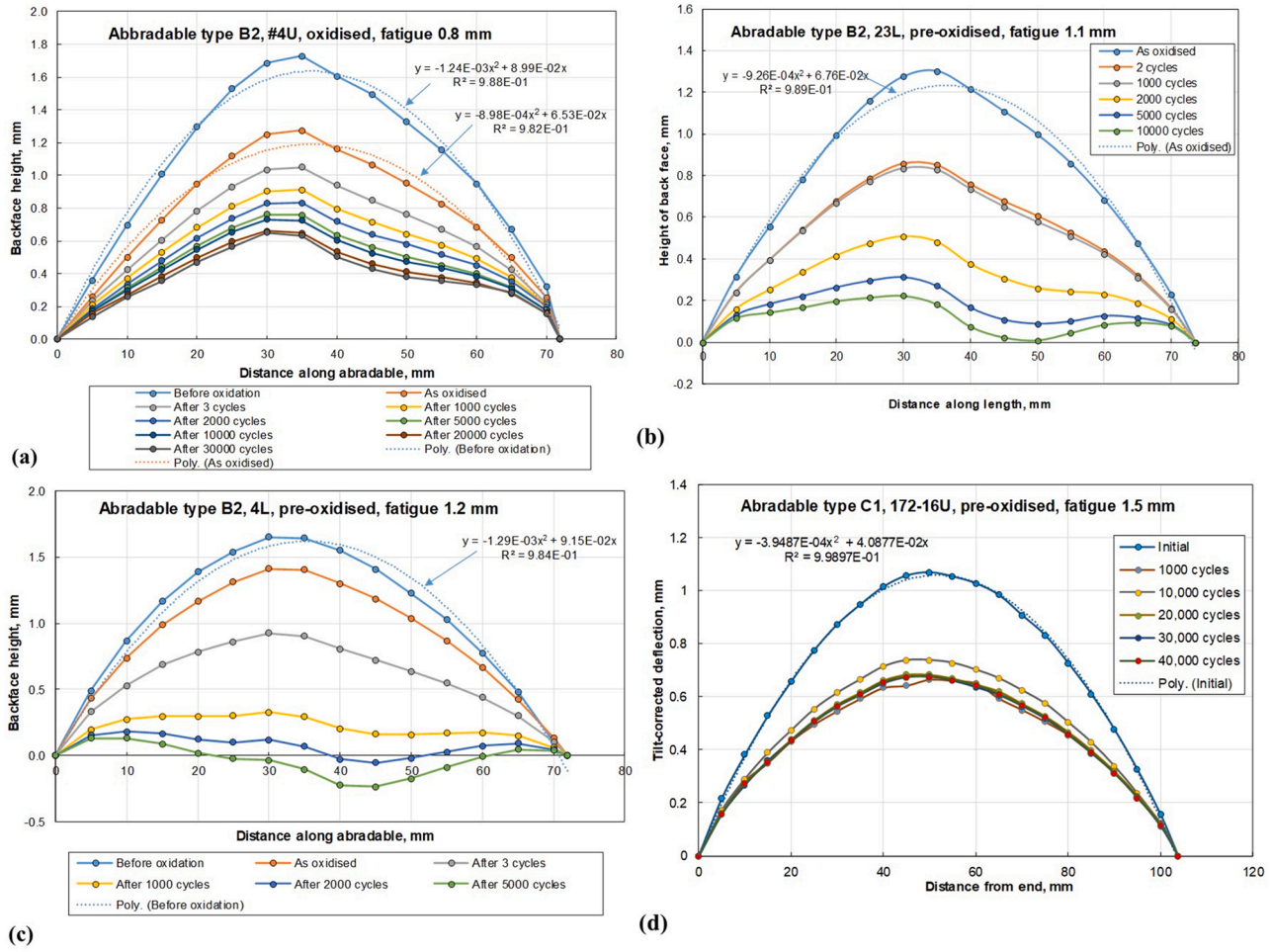

Fig. 13. Test-piece back-face height after a successive group of flexural cycles corresponding to different imposed displacements (δ) for Type B2; (a) 0.8 mm (#4 U), (b) 1.1 mm (#23 U), (c) 1.2 mm (#4 L), (d) Type C1, 1.5 mm (#172_16U).

the abradable layer in the latter having a markedly lower stiffness. One possible reason for the greater modulus in Type A1 compared with Types B1 and B2, arises because of the single-crystal structure in the former that is devoid of the cracks and porosity seen in the LBP-DED build (Types B1 and B2). Notwithstanding that the single crystal structure (CMSX-3) has a lower modulus (~130 GPa) than polycrystalline alloy X in the support structure (~200 GPa), the greater net modulus in Type A1 must imply that the microstructural integrity of the lattice geometry contributes to the overall stiffness.

The other observation that requires explanation is the evolution of the apparent elastic modulus on heating/cooling, most noticeably in the Type C1 specimens and also in the 1st and 2nd heating runs in the un-oxidised Types A1 and B1 specimens. The marked increase in elastic modulus in the case of the un-oxidised specimens points very strongly to the role of residual stresses that are built up within the abradable when the Ni-Al powder in the interstices starts to oxidise to (Ni, Co) O and spinels, as shown in Fig. 9(a) & (b), resulting in a volumetric increase within the interstices, since the Pilling-Bedworth ratio of these oxides is

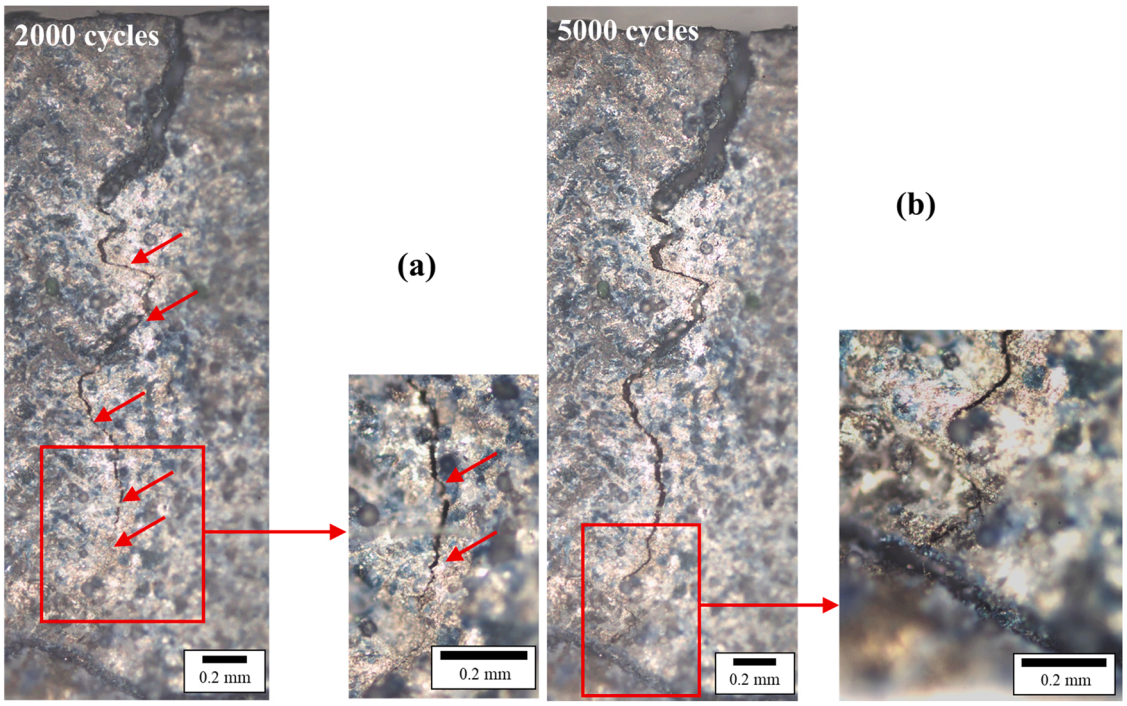

Fig. 14. Optical view of region in side-wall in #4 L ($\delta = 1.2$ mm) located 5.8 mm to the right of centre after; (a) 2000, (b) 5000 flexural cycles.

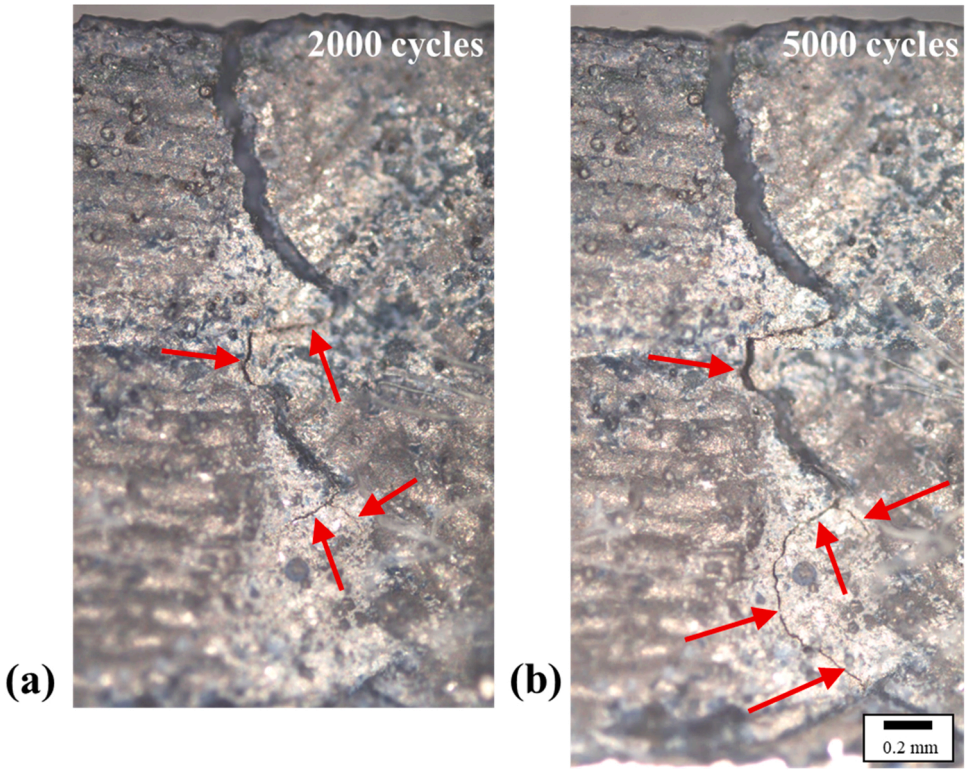

Fig. 15. Optical view of region in side-wall in #4 L ($\delta = 1.2$ mm) located 6.5 mm to the left of centre after; (a) 2000 (b) 5000 flexural cycles.

greater than 1. The volume increase within the interstices results in axial compression of the front and rear lattice walls. This residual stress prevails during cooling and results in a consistently larger value for the elastic modulus during cooling compared with the 1st heating run. The definitive role of residual compressive stresses within the support structure, arising from the volumetric increase accompanying oxidation of Ni-Al within the interstices, can be deduced from Fig. 4(a) and (c). Following annealing in the absence of any Ni-Al in-fill and when viewed from the abradable side, the concave shape of the specimen indicates a shortening of the abradable relative to the substrate. From this change in shape following relaxation, it can be concluded that the support structure must have been in a state of tension following build and subsequent

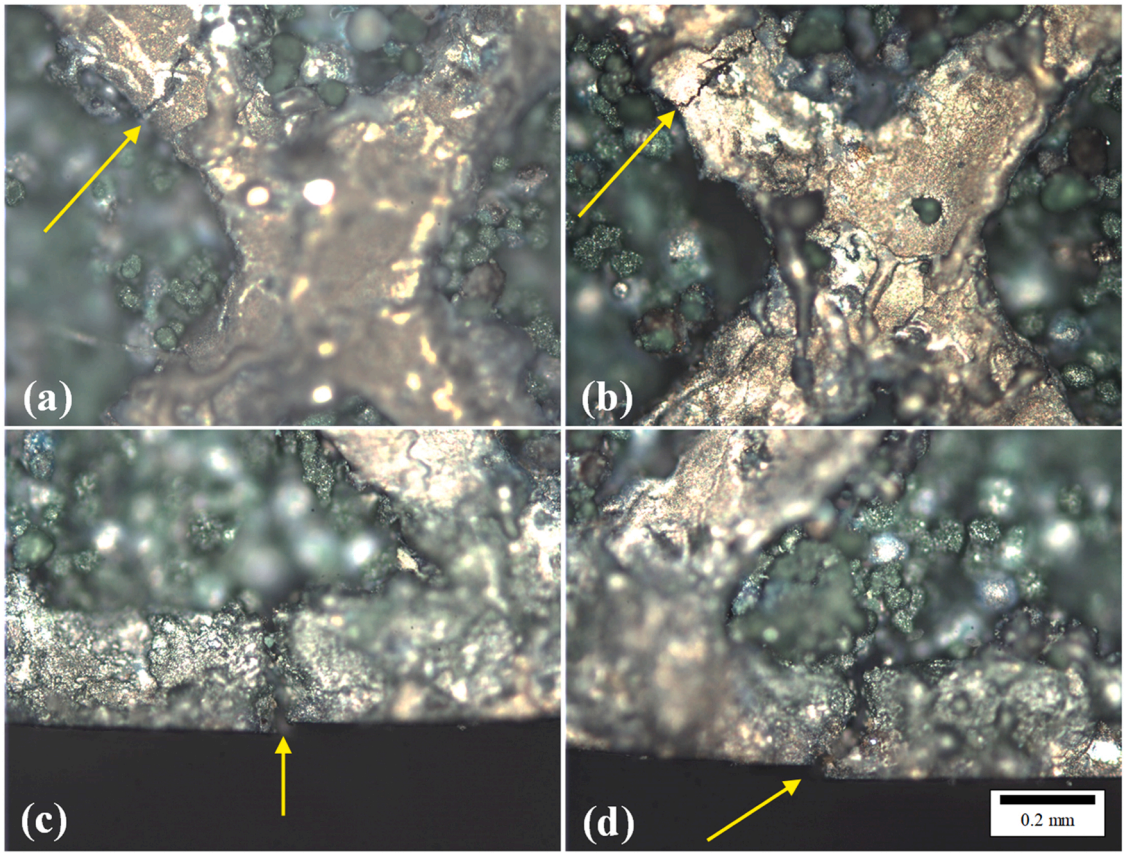

Fig. 16. Optical view of internal nodal structure at the top of the abradable in #5 L ($\delta = 0.8$ mm) after 10,000 flexural cycles; (a) 4 mm to the right of centre, (b) 2 mm to the left of centre in vicinity of side-wall, (c) 5 mm to the left of centre, (d) at the centre in vicinity of side-wall.

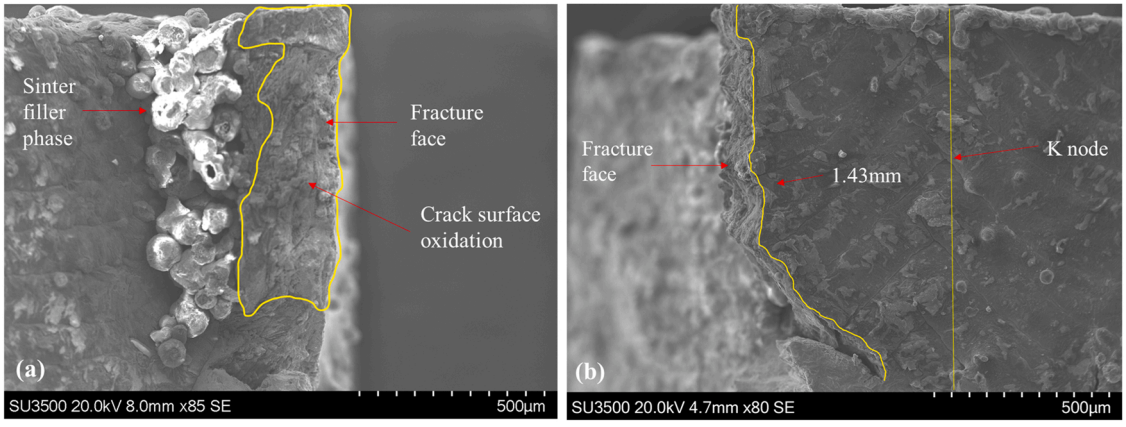

Fig. 17. (a) Secondary electron image of crack face at a K node with oxide layer encompassed within the yellow curve. The examined face corresponds to the fracture surface through the length of front/rear wall (b) Secondary electron image illustrating crack length and geometry from a side view (rotating the crack face by 90° from Fig. 17(a) at a K node). The length of the crack is denoted by the yellow curve.

relaxation during annealing leads to a reduction in tensile stresses through this shape change. However, in the presence of in-fill, the shape change is not only opposite in nature (i.e. convex when viewed from the abradable side) but also markedly greater in magnitude compared with the former. This opposite change in shape must imply that the abradable during subsequent oxidation must have been in a state of compression. The increasing compressive stresses built up within the support structure can only be relaxed by tensile elongation of the abradable. This is achievable for a specimen shape change resulting in an increase in length of abradable relative to the substrate, as observed.

A phenomenological argument based on the residual stress can therefore be invoked to qualitatively account for the dependence of the elastic modulus on the geometry of the support structure, i.e. nodal versus non-nodal (continuous path) design. The entire seal segment was pre-oxidised during which volumetric expansion of Ni-Al during oxidation results in bi-axial compression being set up within the support structure. During cooling, the higher thermal expansion coefficient of the substrate compared with the abradable (support structure and Ni-Al and Ni-Al oxides), results in further compressive stresses developing within the support structure, since the latter is constrained by the rigid substrate. In the case of Type C, some relaxation of residual stresses occurs because of the absence of front/rear walls, but nevertheless there

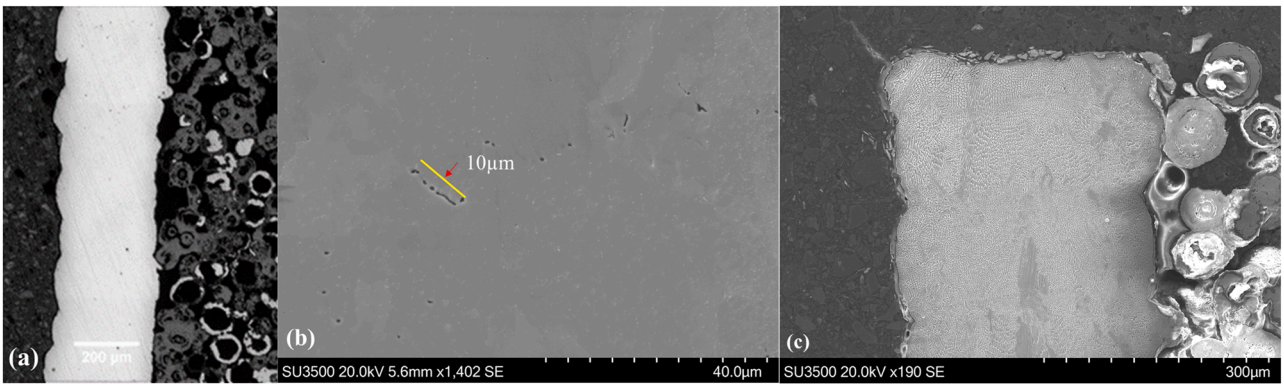

Fig. 18. (a) Low magnification micrograph at the front/rear wall at a K node showing visible porosity (b) Secondary electron image of micro-pores found within close proximity and beginning to concatenate (c) Secondary electron image of the cellular solidification structure at the top of the front/rear support structure.

is still an overall axial constraint owing to the rigid curvature of the substrate comprising the segment. However, when the abradable is extracted from the segment, some of this constraint is eliminated and relaxation occurs within the support structure resulting in flattening (increased radius of curvature). This is greatest for Type C, given the absence of front/rear walls and flattening of the specimen is accompanied by gaps opening between the support structure and Ni-Al and Ni-Al oxides in the interstices. In Types A and B, the relaxation of compressive stresses is significantly lower compared with Type C and any relaxation is concentrated at nodes in the front/rear walls and to a lesser extent within the internal lattice nodes.

While carrying out dynamic modulus measurements, the extracted abradable with underlying substrate (i.e. ~ 1–1.3 mm) is subsequently heated. The higher thermal expansion coefficient of the substrate results in some further relaxation of stresses within the support structure, resulting in a decrease in radius of curvature of the specimen (unflattening). Consequently, the gaps that had "opened up" between interstitial Ni-Al and Ni-Al oxides on cooling now close, thereby resulting in an "effective" contact of the interstitial species with the support structure walls. In the absence of front/rear walls, this closing up of gaps between interstitial Ni-Al and Ni-Al oxides and the support structure in Type C abradables effectively increases the stiffness of the test-piece, accounting for the observations in Fig. 8(e) and (f). In specimens of Types A and B, the front/rear walls primarily contribute to the elastic modulus and the above effect is only secondary. Therefore, the variation of out-of-plane flexural modulus follows the usual temperature dependence, as in Fig. 8(a) – (d).

The apparent Young's modulus of the abradable in the out-of-plane vibration direction plays a key role in the four-point bending fatigue tests, which is observed most noticeably for Type B1 specimens. From Fig. 10 it can be observed that for an imposed deflection, $\delta \leq 0.8$ mm, beyond an initial decrease in elastic modulus after a number of flexural cycles, the decrease thereafter is small, but for $\delta \geq 1.1$ mm there is a rapid decline over a smaller number of cycles. The decreasing apparent elastic modulus with an increasing number of cycles accompanied by the flattening of the specimen is a manifestation of inelastic (plastic) deformation within the support structure. This can be deduced from the quasi-static loading conditions in Fig. 11(a) – (f). The non-linearity in the load-displacement plot is a clear indication of accumulating damage/cracking within the support structure. For both displacements it is clear that cracking is occurring during the loading cycle, which accounts for the offset between loading/unloading curves. For $\delta = 0.8$ mm, a marked offset is observed only after the first loading cycle, while for $\delta = 1.1$ mm, a significant offset occurs up to the onset of 1000 flexural cycles, i.e. the 1,001st. The decrease in peak load is gradual for $\delta = 0.8$ mm (~ 150 N) over 20,000 cycles, but for $\delta = 1.1$ mm the decrease is steep between 1000 and 5000 cycles (~ 200 N) with a smaller further decrease (~ 30 N) thereafter to 20,000 cycles. In the latter, the quasi-static apparent elastic modulus is ~ 30–35 GPa lower than the dynamic modulus; Fig. 10 and Fig. 12(b). These facts coupled with the marked change in specimen curvature; Fig. 13(b) beyond 1000 cycles indicates that significant plastic deformation occurs within the abradable, which must be related to stress concentrations leading to extensive cracking. Therefore, a rapid decrease in the dynamic elastic modulus is concomitant with a significant decrease in the maximum applied load as well as a marked change in specimen curvature. This criterion can be used to examine fatigue tests for the range of displacements and support structure design. For higher imposed deflection ($\delta = 1.2$ mm) a rapid decrease in dynamic elastic modulus occurs beyond 5 cycles (Fig. 10) and this is also accompanied by a rapid change in specimen curvature (as also seen in Fig. 13(c) beyond 5 cycles). For lower imposed deflection ($\delta \leq 0.8$ mm) or for continuous path design ($\delta \leq 1.5$ mm), there is neither a marked change in specimen curvature nor a decrease in dynamic elastic modulus, which indicates minimal degradation of the abradable.

The accumulation of damage within the abradable during bending will be within the support structure. During bending, the front/rear walls in case of the lattice support structure experience tensile stresses, which are highest at the outer layers of the abradable in the vicinity of the surface. In the Type B2 specimens, the pre-existing solidification fissures within the front/rear walls act as stress concentration features and nucleate cracks. With the growth of a few localised cracks within the front/rear walls, stress concentrations develop which focuses further deformation at such cracks, subsequently shielding areas in the vicinity. The rate of degradation is thus likely to be controlled by the density of such wall defects. It is pertinent to note that damage within the internal lattice only occurs to a limited extent; as shown in Fig. 16(a) – (d), with some cracks at the vicinity of X-nodes having grown to intersect the abradable surface, indicating that the internal lattice structure can be envisaged as being axially more compliant than the front/rear walls. In the absence of front/rear walls and the internal nodal lattice structure, as in the continuous path, Type C1, for an equivalent change in specimen curvature, there is no discernible damage within the abradable. Also, in the absence of solidification defects within the front/rear walls, as in a single crystal front/rear wall, there is no discernible damage observed within the abradable also for an equivalent change in specimen curvature, as seen in the Type A1 structures.

The current flexural tests were performed at RT. Nevertheless, they elucidate implications of the support structure design on the out-of-plane flexure modulus, which in turn affects the nucleation and propagation of cracks during cyclic loading. Specifically, it has been shown that in the absence of front/rear walls and internal lattice nodes there is a marked decrease in out-of-plane flexure modulus owing to the lower residual stresses within the abradable. Furthermore, in the case of a lattice support structure, the propagation of cracks from solidification fissures in the front/rear walls is accompanied by a changing specimen

curvature and concomitantly accompanied by a decrease in out-of-plane flexure modulus.

5. Conclusions

From this research, the following conclusions can be drawn:

(1) The inhomogeneous abradable structure results in the axial apparent dynamic elastic modulus being dependent on the direction of vibration; it is lowest for out-of-plane flexure and highest for in-plane flexure.
   (i) At room temperature, the abradable forward and rear walls and internal nodes in Types A1, Type B1 and B2 contribute significantly to the apparent elastic modulus in out-of-plane flexure (E ~ 10 – 20 GPa), while in the absence of forward and rear walls in case of the continuous path support structure, Type C1, the abradable contributes little to the overall stiffness (E ~ 0.1 GPa).
   (ii) Oxidation of the Ni-Al infill sinter results in internal stresses developing within the abradable with an increase in elastic modulus. This is most prominent in the continuous path design, Type C1, where a two-fold increase in apparent elastic modulus occurs in out-of-plane flexure.

(2) Four-point bending was used to study the implications of the elastic modulus of the abradable under fatigue. There is a decrease in elastic modulus with increasing flexural cycles and a concomitant increase in radius of curvature (flattening).
   (i) A threshold displacement for Type B2 abradables was identified ($\delta \geq 1.1$ mm), beyond which there is a rapid decrease in elastic modulus after a given number of flexural cycles. For increasing displacement, this occurred at a lower number of cycles. No such degradation was observed up to 40,000 cycles for equivalent changes in curvatures in the Type A1 and Type C1 specimens.
   (ii) In the Type B2 abradable specimens, deformation was mainly restricted to the forward and rear walls where cracking was observed. Cracks nucleated at LBP-DED solidification shrinkage fissures and propagated either to the surface or towards the base of the abradable. Coalescence of cracks was also observed at closely located fissures. Limited cracking was observed within the internal lattice nodes.

CRediT authorship contribution statement

Roger Morrell: Writing – original draft, Validation, Methodology, Formal analysis. **Zachariah Nye:** Methodology, Data curation. **Simon Donovan:** Investigation, Formal analysis, Conceptualization. **Peter Daum:** Validation, Investigation, Formal analysis, Conceptualization. **Neil D'Souza:** Writing – original draft, Supervision, Project administration, Methodology, Investigation, Funding acquisition, Formal analysis, Data curation, Conceptualization. **Siddharth Ravichandran:** Methodology, Investigation, Formal analysis, Conceptualization. **Robert Lancaster:** Writing – original draft, Supervision, Methodology.

Declaration of Competing Interest

The authors declare that they have no known competing financial interests or personal relationships that could have appeared to influence the work reported in this paper.

Data Availability

The raw/processed data required to reproduce these findings cannot be shared at this time as the data also forms part of an ongoing study.

Acknowledgments

In-kind support and the supply of material was gratefully provided by Rolls-Royce plc.

References

[1] A. Uriondo, M. Esperon-Miguez, S. Perinpanayagam, The present and future of additive manufacturing in the aerospace sector: a review of important aspects, *Proc. Inst. Mech. Eng., Part G: J. Aerosp. Eng.*, 229 (2015) 2132 – 2147.
[2] ISO/ASTM 52900, Additive Manufacturing – General Principles – Terminology, International Organisation for Standardisation, Geneva, Switzerland, 2015.
[3] N. Shamsaei, A. Yadollahi, L. Bian, S. Thompson, A overview of direct laser deposition for additive manufacturing part II: mechanical behaviour, process parameter optimisation and control, Addit. Manuf. 8 (2015) 12–35.
[4] A. Yadollahi, N. Shamsaei, S. Thompson, D. Seely, Effects of process time interval and heat treatment on the mechanical and microstructural properties of direct laser deposited 316L stainless steel, *Mater. Sci. Eng., A* 644 (2015) 171–183.
[5] W. Frazier, Metal additive manufacturing review, J. Mater. Eng. Perform. 23 (2011) 1413.
[6] B. Onuike, A. Bandyopadhyay, Additive manufacturing of Inconel 718 – Ti6Al4V bimetallic structures, Addit. Manuf. 22 (2018) 844–851.
[7] M. Akbari, R. Kovacevic, An investigation on mechanical and microstructural properties of 316LSi parts fabricated by a robotized laser/wire direct metal deposition system, Addit. Manuf. 23 (2018) 487–497.
[8] A. Harooni, M. Iravani, A. Khajepour, J.M. King, A. Khalifa, A.P. Gerlich, Mechanical properties and microstructures in zirconium deposited by injected powder laser additive manufacturing, Addit. Manuf. 22 (2018) 537–547.
[9] C. Schneider-Maunoury, L. Weiss, P. Acquier, D. Boisselier, P. Laheurte, Functionally graded Ti6Al4V-Mo alloy manufactured with DED-CLAD® process, Addit. Manuf. 17 (2017) 55–66.
[10] Y. Koizumi, A. Okazaki, A. Chiba, T. Kato, A. Takezawa, Cellular lattices of biomedical Co-Cr-Mo alloy fabricated electron beam melting with the aid of shape optimization, Addit. Manuf. 12 (2016) 305–313.
[11] R. Mahshid, H.N. Hansen, K.L. Hobjerra, Strength analysis and modelling of cellular lattice structures manufactured using selective laser melting for tooling operations, Mater. Des. 104 (2016) 276–283.
[12] P. Li, Z. Wang, N. Petrinic, C.R. Siviour, Deformation behaviour of stainless steel microlattice structures by selective laser melting, Mater. Sci. Eng. A 614 (2014) 116–121.
[13] P. Baronowski, P. Płatek, A. Antolak-Dudka, et al., Deformation of honeycomb cellular structures manufactured with laser engineered net shaped (LENS) technology quasi-static loading; experimental testing and simulation, Addit. Manuf. 25 (2019) 307–316.
[14] F. Brenne, T. Niendorf, H.J. Maier, Additively manufactured cellular structures: Impact of microstructure and local strains on the monotonic and cyclic behaviour under uniaxial and bending load, J. Mater. Proc. Tech. 213 (2013) 1558–1564.
[15] L. Yang, S. Wu, C. Yan, P. Chen, L. Zhang, C. Han, C. Cai, S. Wen, Y. Zhou, Y. Shi, Fatigue properties of Ti-6Al-4V Gyroid graded lattice structures fabricated by laser powder bed fusion with lateral loading, Addit. Manuf. 46 (2021), 102214.
[16] L. Yang, C. Yan, W. Cao, Z. Liu, B. Song, S. Wen, C. Zhang, Y. Shi, S. Yang, Compression-compression fatigue behaviour of gyroid-type triply periodic minimal surface porous structures fabricated by selective laser melting, Acta Mater. 181 (2019) 49–66.
[17] A. Saboori, A. Aversa, G. Marchese, S. Biamino, M. Lombardi, P. Fino, Application of Directed Energy Deposition-Based Additive Manufacturing in Repair, Appl. Sci. 9 (16) (2019) 3316.
[18] P. Daum, S. Donovan, S. Ravichandran, Abradable Sealing Element. United States Patent US2021156312AA.
[19] P. Daum, S. Donovan, C. Heason, Wall Deposition. United States Patent US2021254489AA.
[20] S. Timoshenko, Analysis of bi-metal thermostats, J. Opt. Soc. Am. 11 (1925) 233–255.
[21] P. Hähner, C. Rinaldi, V. Bicego, et al., Research and development into a European code-of-practice strain-controlled thermo-mechanical fatigue testing, Int. J. Fatigue 30 (2008) 372–381.
[22] Standard test method for dynamic Young's modulus, shear modulus and Poisson's ratio by sonic resonance, ASTM: E1875 – 08 and E1876 – 09.
[23] W.C. Young, R.G. Budynas. Roark's Formulas for Stress and Strain, seventh ed., McGraw Hill, 2002.
[24] R. Morrell, A National Measurement Good Practice Guide, No. 7, Flexural strength testing of ceramics and hard materials, National Physical Laboratory (1997).
[25] Y.W. Bao, Y.C. Zhou, X.X. Bu, Y. Qiu, Evaluating elastic modulus and strength of hard coatings by relative method, *Mater. Sci. Eng., A* 458 (2007) 268–274.
[26] W. Hermann, H.G. Sockel, J. Han, A. Betram, Elastic properties and determination of elastic constants of Ni-base superalloys by a free-beam technique, *Superalloys 1996*, eds. R. D. Kissinger *et. al.*, The Min. Met. Mater. Soc., (1996) 229 – 238.
[27] L.N. McCartney, C. Clay, Rigorous analysis for estimation the orientation of cubic, Cryst. NPL Rep. Mat. 30 (2009).
[28] R. Morrell, Elastic Modulus Measurements on Single Crystal Turbine Alloy, CM186LC, NPL Report E030200133, 2003.